1 **Constraining frequency-magnitude-area relationships for rainfall and flood**

2 **discharges using radar-derived precipitation estimates: Example applications in the**

3 **Upper and Lower Colorado River Basins, U.S.A.**

4 Caitlin A. Orem*, Jon D. Pelletier

5 [1] {Department of Geosciences, The University of Arizona, 1040 E. 4th Street, Tucson,

6 AZ 85721, USA}

7 Correspondence to: C.A. Orem (oremc@email.arizona.edu)

8

9 **Abstract**

10 Flood-envelope curves (FEC) are useful for constraining the upper limit of possible flood

11 discharges within drainage basins in a particular hydroclimatic region. Their usefulness,

12 however, is limited by their lack of a well-defined recurrence interval. In this study we

13 use radar-derived precipitation estimates to develop an alternative to the FEC method, i.e.

14 the frequency-magnitude-area-curve (FMAC) method, that incorporates recurrence

15 intervals. The FMAC method is demonstrated in two well-studied U.S. drainage basins,

16 i.e. the Upper and Lower Colorado River basins (UCRB and LCRB, respectively), using

17 Stage III Next-Generation-Radar (NEXRAD) gridded products and the diffusion-wave

18 flow-routing algorithm. The FMAC method can be applied worldwide using any radar-

19 derived precipitation estimates. In the FMAC method, idealized basins of similar

20 contributing area are grouped together for frequency-magnitude analysis of precipitation

21 intensity. These data are then routed through the idealized drainage basins of different

22 contributing areas, using contributing-area-specific estimates for channel slope and

23 channel width. Our results show that FMACs of precipitation discharge are power-law

24 functions of contributing area with an average exponent of 0.82 ± 0.06 for recurrence

25 intervals from 10 to 500 years. We compare our FMACs to published FECs and find that

26 for wet antecedent-moisture conditions, the 500-year FMAC of flood discharge in the

27 UCRB is on par with the U.S. FEC for contributing areas of $\sim 10^2$ to 10^3 km^2. FMACs of

28 flood discharge for the LCRB exceed the published FEC for the LCRB for contributing

29 areas in the range of $\sim 10^3$ to 10^4 km^2. The FMAC method retains the power of the FEC

30 method for constraining flood hazards in basins that are ungauged or have short flood

31 records, yet it has the added advantage that it includes recurrence interval information

32 necessary for estimating event probabilities.

33

34 **1.   Introduction**

35 **1.1 Flood-Envelope Curves**

36   For nearly a century, the flood-envelope curves (FEC), i.e. a curve drawn slightly

37 above the largest measured flood discharges on a plot of discharge versus contributing

38 area for a given hydroclimatic region (Enzel et al., 1993), have been an important tool for

39 predicting the magnitude of potential future floods, especially in regions with limited

40 stream-gauge data. FECs assume that, within a given hydroclimatic region, maximum

41 flood discharges for one drainage basin are similar to those of other drainage basins of

42 the same area, despite differences in relief, soil characteristics, slope aspect, etc. (Enzel et

43 al., 1993). This assumption enables sparse and/or short-duration flood records over a

44 hydroclimatic region to be aggregated in order to provide more precise constraints on the

45 magnitude of the largest possible (i.e. long-recurrence-interval) floods.

46   FECs reported in the literature have a broadly similar shape across regions of

47 widely differing climate and topography. For example, FECs for the Colorado River

48 Basin (Enzel et al., 1993), the central Appalachian Mountains (Miller, 1990; Morrison

49 and Smith, 2002), the 17 hydrologic regions within the U.S. defined by Crippen and Bue

50 (1977), the U.S. as a whole (Costa, 1987; Herschy, 2002), and China (Herschy, 2002) are

51 all concave-down when plotted in log-log space, with maximum recorded flood

52 discharges following a power-law function of contributing area for small contributing

53 areas and increasing more slowly at larger contributing areas (i.e. the curve "flattens").

54   Traditional FECs also have the potential problem that the maximum flood

55 associated with smaller drainage basins may be biased upward (or the floods of larger

56 drainage basins biased downward) because there are typically many more records of

57 floods in smaller drainage basins relative to larger drainage basins (because there are

58 necessarily fewer large drainage basins in any hydroclimatic region). That is, the largest

59 flood of record for small drainage basins within a hydroclimatic region likely corresponds

60 to a flood of a larger recurrence interval compared with the largest flood of record for

61 larger drainage basins. In this paper we present a method that includes recurrence-interval

62 information and avoids any sample-size bias that might exist as a function of contributing
63 area.

64   The use of FECs to quantify flood regimes is limited by the lack of recurrence-
65 interval information (Wolman and Costa, 1984; Castellarin et al., 2005) and by the short
66 length, incomplete nature, and sparseness of many flood discharge records. Without
67 recurrence-interval information, the data provided by FECs are difficult to apply to some
68 research and planning questions related to floods. In the U.S. for example, the 100- and
69 500-year flood events are the standard event sizes that define flood risk for land planning
70 and engineering applications (FEMA, 2001).

71   Previously published studies have looked at new approaches to approve upon the
72 FEC method. Castellarin et al. (2005) took a probabilistic approach to estimating the
73 exceedance probability of the FEC for synthetic flood data. The authors were able to
74 relate the FECs of certain recurrence intervals to the correlation between sites, the
75 number of flood observations, and the length of each observation. Later, Castellarin
76 (2007) and Castellarin et al. (2009) applied these methods to real flood record data and
77 extreme rainfall events for basins within north-central Italy. Castellarin et al. (2009) also
78 created depth-duration envelope curves of precipitation to relate extreme precipitation
79 events to mean annual precipitation. This group of studies was successful in
80 incorporating recurrence-interval information into the traditional FEC method. However,
81 most of the models presented in these studies were completed with synthetic data or
82 created for design storm processes and require additional analysis. Also, most of the
83 precipitation data used in these past studies was collected using rain gauges (point
84 sources), while only a small subset of data in Castellarin et al. (2009) was sourced from
85 radar-derived precipitation estimates. In contrast to these studies we formulate a
86 simplified method (i.e. the FMAC method) that is readily applicable to any region of
87 interest and can be directly compared to already existing FECs. Also we favor the use of
88 spatially complete radar-derived precipitation estimates in order to apply our methods to
89 ungauged basins.

90   To mitigate the uncertainty caused by short and incomplete flood discharge
91 records, this study uses a space-for-time substitution (e.g. regionalization) to lengthen the
92 record for a given contributing area. Previous studies have employed similar methods,

including the index-flood procedure first described by Dalyrymple (1960) and expanded upon by many subsequent authors. The index-flood method uses data from multiple sites within a region to construct more accurate flood-quantile estimates than would be possible using a single site (Stedinger et al., 1993 and Hosking and Wallis, 2005). This method can also be used on precipitation data where it is referred to as the station-year method (Buishand, 1991). The index-flood method is based on two major assumptions: (1) that observations from two or more basins are independent; and (2) that observations follow the same distribution (Wallis et al., 2007).

Here we use a regionalization method similar to the index-flood method in order to calculate rainfall intensity values associated with specific recurrence intervals. The assumption of statistical independence of rainfall (and associated flood) observations is one that we assume in this study but understand may not be true for all samples in our natural data set. This assumption is difficult to definitively prove with natural data (Hosking and Wallis, 2005). For example, a large rainfall event may affect two basins in a similar way and therefore create correlated maximum rainfall intensity values. This spatial correlation is difficult to avoid and may cause biased results. However, it has been shown that the index-flood method can be used in the absence of fully statistically independent observations and still give robust results (Hosking and Wallis, 1988; Hosking and Wallis, 2005). The assumption that observations are sampled from the same distribution is also somewhat difficult to prove with natural data, but by knowing the study areas well a researcher can identify regions with similar rainfall and flood mechanisms. Many examples of this type of area analysis can be found in the literature, including Soong et al. (2004) who separated rural streams in Illinois into hydrological regions based on basin morphology and soil characteristics. Soong et al. (2004) used regionalization in their study to increase the amount of flood data available for frequency analysis. Wallis et al. (2007) employed a similar regionalization method to identify hydroloclimatic regions in their study of precipitation frequency in Washington. It should be noted that FEC's in general use this type of regionalization approach to analyze maximum flood data for hydroclimatic regions with similar flood mechanisms. In this study we similarly attempt to analyze regions based on their basic rainfall mechanisms, in this case by separating the Upper and Lower Colorado River basins.

124   In this study, a new method for estimating flood discharges associated with user-
125   specified recurrence intervals is introduced that uses radar-derived precipitation estimates
126   (in this case rainfall only), combined with the diffusion-wave flow-routing algorithm, to
127   create frequency-magnitude-area curves (FMACs) of flood discharge. Our method (i.e.
128   the FMAC method) retains the power of the FEC approach in that data from different
129   drainage basins within a hydroclimatic region are aggregated by contributing area,
130   thereby enabling large sample sizes to be obtained within each contributing-area class in
131   order to more accurately constrain the frequencies of past extreme flood events and hence
132   the probabilities of future extreme flood events within each class. The method improves
133   upon the FEC approach in that the complete spatial coverage of radar-derived
134   precipitation estimates provides for large sample sizes of most classes of contributing
135   area (larger contributing areas have fewer samples). The radar-derived precipitation
136   estimates include only rainfall and therefore snow and other types of precipitation are not
137   included in the study. The precipitation estimates are then used to predict flood
138   discharges associated with specific recurrence intervals by first accounting for water lost
139   to infiltration and evapotranspiration using runoff coefficients appropriate for different
140   contributing areas and antecedent-moisture conditions, and then routing the available
141   water using a flow-routing algorithm. Predicted flood discharges are presented as FMACs
142   on log-log plots, similar to traditional FECs, except that the method predicts a family of
143   curves, one for each user-defined recurrence interval. These plots are then compared to
144   FECs for the study region (Enzel et al., 1993) and the U.S. (Costa, 1987).
145

146   **1.2 Study Area**
147   This study focuses on the Upper and Lower Colorado River Basins (UCRB and
148   LCRB, respectively; Fig. 1) as example applications of the FMAC method. Although the
149   methods we develop are applied to the UCRB and LCRB in the western U.S. in this
150   study, the methods are applicable to any region of interest where radar-derived
151   precipitation estimates are available (i.e. the entire U.S. and at least 22 countries around
152   the world; Li, 2013; RadarEU, 2014). We focus on the UCRB and LCRB because they
153   have been a focus of flood-hazard assessment studies in the western U.S. and hence the
154   FECs available for them are of especially high quality. In addition, the distinctly different

155 hydroclimatic regions of the UCRB and LCRB (Sankarasubramanian and Vogel, 2003)

156 make working in these regions an excellent opportunity to test and develop the new

157 methods of this study on different precipitation patterns and storm types.

158   Precipitation and flooding in the LCRB are caused by convective-type storms,

159 including those generated by the North American Monsoon (NAM), and frontal-type and

160 tropical storms sourced from the Pacific Ocean and the Gulf of California (House and

161 Hirschboeck, 1997; Etheredge et al., 2004). In the UCRB, the influence of the NAM and

162 tropical storms is diminished and floods are generally caused by Pacific frontal-type

163 storms (Hidalgo and Dracup, 2003). In both regions, the El Niño Southern Oscillation

164 (ENSO) alters the frequency and intensity of the NAM, tropical storms, and the Pacific

165 frontal systems, and can cause annual variations in precipitation and flooding (House and

166 Hirschboeck, 1997; Hidalgo and Dracup, 2003). Winter storms in both regions are also

167 intensified by the occurrence of atmospheric rivers (Dettinger et al., 2011), which can

168 cause total winter precipitation to increase up to approximately 25% (Rutz and

169 Steenburgh, 2012). The radar-derived precipitation estimates used in this study record

170 this natural variability in precipitation in the two regions.

171   The methods used in this study to calculate rainfall and flood discharges of

172 specified recurrence intervals from radar-derived precipitation estimates require a few

173 main assumptions. The first assumption is that of climate stationarity, i.e. the parameters

174 that define the distribution of floods do not change through time (Milly et al., 2008).

175 Climate is changing and these changes pose a challenge to hazard predictions based on

176 the frequencies of past events. Nevertheless, stationarity is a necessary assumption for

177 any probabilistic analysis that uses past data to make future predictions. The results of

178 such analyses provide useful starting points for more comprehensive analyses that

179 include the effects of future climate changes. The second assumption is that the sample

180 time interval is long enough to correctly represent the current hydroclimatic state (and its

181 associated precipitation patterns and flood magnitudes and risks) of the specified study

182 area. Our study uses data for the 1996 to 2004 water years and therefore may be limited

183 by inadequate sampling of some types of rare weather patterns and climate fluctuations

184 within that time interval. To address whether or not the sample time interval used in this

185 study includes major changes in circulation and weather patterns, and therefore is a good

186   representation of climate in the CRB, we investigated the effect of the El Niño Southern

187   Oscillation (ENSO) on rainfall intensity within the UCRB and LCRB. ENSO is a well-

188   known important influence on the hydroclimatology of the western U.S. (Hidalgo and

189   Dracup, 2003; Cañon et al., 2007). In general, winter precipitation in the southwestern

190   U.S. increases during El Niño events and decreases during La Niña events (Hidalgo and

191   Dracup, 2003). The opposite effects are found in the northwestern portions of the U.S.

192   (including the UCRB; Hidalgo and Dracup, 2003). The last assumption of the method is

193   that all basins of similar contributing area respond similarly to input rainfall, i.e. that they

194   have similar flood-generating and flow-routing mechanisms. Specifically, the method

195   assumes that basins of similar contributing area have the same runoff coefficient, flow-

196   routing parameters, basin shape, and channel length, width, and slope. This assumption is

197   necessary in order to aggregate data into discrete contributing-area classes so that the

198   frequency of extreme events can be estimated from relatively short-duration records. In

199   this study, high-recurrence-interval events (i.e. low frequency events) can be considered

200   despite the relatively short length of radar-derived-precipitation-estimate records because

201   the number of samples in the radar-derived record is extremely large, especially for small

202   contributing areas and small duration floods. For example, for a 1-h time-interval-of-

203   measurement and a contributing area of 4,096 km^2 event in the UCRB, there are

204   approximately 40 (number of spatial scale samples) times 55000 (number of temporal

205   scale samples in nine years of data) samples of rainfall-intensity values (and associated

206   modeled discharges obtained via flow routing). As contributing area and time intervals of

207   measurement increase there are successively fewer samples, within any particular

208   hydroclimatic region, thus increasing the uncertainty of the resulting probability

209   assessment for larger areas and longer time periods.

210

211   **2.   Next-Generation-Radar (NEXRAD) Data**

212   The specific radar-derived precipitation estimates we use in this study come from

213   the Stage III Next-Generation-Radar (NEXRAD) gridded product, which is provided for

214   the entire U.S., Guam, and Puerto Rico. NEXRAD was introduced in 1988 with the

215   introduction of the Weather Surveillance Radar 1988 Doppler, or WSR-88D, network

216   (Fulton et al., 1998). The WSR-88D radars use the Precipitation Processing System

217 (PPS), a set of automated algorithms, to produce precipitation intensity estimates from

218 reflectivity data. Reflectivity values are transformed to precipitation intensities through

219 the empirical *Z-R* power-law relationship,

220 $Z = \alpha R^\beta$ (1)

221 where Z is precipitation rate (mm h^{-1}), α and β are derived empirically and can vary

222 depending on location, season, and other conditions (Smith and Krajewski, 1993), and R

223 is reflectivity (mm^6 m^{-3}; Smith and Krajewski, 1993; Fulton et al., 1998; Johnson et al.,

224 1999). Precipitation intensity data are filtered and processed further to create the most

225 complete and correct product (Smith and Krajewski, 1993; Smith et al., 1996; Fulton et

226 al., 1998; Baeck and Smith, 1998). Further information and details about PPS processing

227 are thoroughly described by Fulton et al. (1998).

228   Stage III NEXRAD gridded products are Stage II precipitation products mapped

229 onto the Hydrologic Rainfall Analysis Project (HRAP) grid (Shedd and Fulton, 1993).

230 Stage II data are hourly precipitation intensity products that incorporate both radar

231 reflectivity and rain-gauge data (Shedd and Fulton, 1993) in an attempt to make the most

232 accurate precipitation estimates possible. The HRAP grid is a polar coordinate grid that

233 covers the conterminous U.S., with an average grid size is 4 km by 4 km, although grid

234 size varies from approximately 3.7 km (north to south) to 4.4 km (east to west) in the

235 southern and northern U.S., respectively (Fulton et al., 1998).

236

237 3. Methods

238 3.1 NEXRAD Data Conversion and Sampling

239   NEXRAD Stage III gridded products (hereafter NEXRAD products) for an area

240 covering the Colorado River basin from 1996 to 2005 were downloaded from the NOAA

241 HDSG website (http://dipper.nws.noaa.gov/hdsb/data/nexrad/cbrfc_stageiii.php) for

242 analysis. The data files were converted from archived XMRG files to ASCII format (each

243 data file representing the mean rainfall intensity within each 1 h interval) using the

244 xmrgtoasc.c program provided on the NOAA HDSG website. The ASCII data files were

245 then input into a custom program written in IDL for analysis.

246

247 3.2 Rainfall Sampling Over Space

In this study we quantified hourly rainfall intensities (mm h^{-1}) over square idealized drainage basins (i.e. not real drainage basins, but square drainage basins as shown schematically in Fig. 2A as brown squares) of a range of areas from 16 km^2 to 11,664 km^2 (approximately the contributing area of the Bill Williams River, AZ, for readers familiar with the geography of the western U.S.) by successively spatially averaging rainfall-intensity values at HRAP pixel-length scales of powers of two (e.g. 4, 16 pixel^2, etc.) and three (e.g. 9, 81 pixel^2, etc.; Fig. 2, Step 1). Spatial averaging is done by both powers of 2 and 3 simply to include more points on the FMACs than would result from using powers of 2 or 3 alone. The number of samples within each contributing area class limited the range of contributing areas used in this study, i.e. at larger contributing areas there were too few samples to successfully apply the frequency analysis.

UCRB and LCRB boundaries from GIS hydrologic unit layers created by the USGS and provided online through the National Atlas site (http://www.nationalatlas.gov/atlasftp.html#hucs00m) were projected to HRAP coordinates using the methods of Reed and Maidment (2006). These boundaries were used to delineate the region from which rainfall data were sampled from the NEXRAD products, i.e. when averaging rainfall data by powers of two and three a candidate square drainage basin was not included in the analysis if any portion of the square fell outside of the boundaries of the UCRB or LCRB (Fig. 2A). Throughout the analysis, the HRAP pixel size was approximated by a constant 4 km by 4 km size despite the fact that HRAP pixel sizes vary slightly as a function of latitude (Reed and Maidment, 2006). Our study's drainage basins span latitudes between approximately 31°N and 43°N resulting in a maximum error of 15%. However, by keeping the pixel size constant, all pixels could be treated as identical in size and shape allowing us to sample the NEXRAD products in an efficient and automated way over many spatial scales.

For larger contributing areas, necessarily fewer samples are available within a given hydroclimatic region, thus increasing the uncertainty associated with the analysis for those larger contributing-area classes. For the UCRB and LCRB specifically, the uncertainty in the analysis becomes significant for contributing-area classes equal to and larger than ~10^3 to 10^4 km^2 depending on the recurrence interval being analyzed. Of

279 course, if the hydroclimatic region is defined to be larger, more samples are available for
280 each contributing-area class and hence larger basins can be analyzed with confidence.
281
282 **3.3 Rainfall Sampling Over Time**
283   In addition to computing rainfall intensities as a function of spatial scale, we
284 averaged rainfall intensities as a function of the time interval of measurement ranging
285 from 1 to 64 hours in powers of two by averaging hourly rainfall intensity records over
286 the entire 9-year study period (Fig. 2, Step 1). This range in time intervals was chosen in
287 order to capture rainfall events that last on the order of ~1 hour (convective-type storms)
288 to days (frontal-type storms).
289   Rainfall data was sampled temporally by taking the maximum value of each storm
290 event. Storm events were identified as consecutive non-zero rainfall intensity values
291 separated by instances of zero values in time for each temporal scale. This allows for
292 multiple maximum rainfall values in time to be sampled within a year and throughout the
293 entire 9-year study period. This sampling method is similar to that used in the Peak Over
294 Threshold (POT) method typically used on discharge data where a minimum threshold
295 value is set and maximum peaks above the threshold value are recorded as maximum
296 events. Here we set the minimum threshold value to zero and hence the maximum values
297 of all individual storm events are considered in the analysis.
298
299
300 **3.4 Rainfall Recurrence Interval Calculations**
301   To determine the rainfall-intensity values with a user-specified recurrence
302 interval, maximum rainfall intensities of storm events sampled from the NEXRAD data
303 for each contributing-area and time-interval-of-measurement class were first ranked from
304 highest to lowest (Fig. 2A, Step 2). The relationship between recurrence intervals and
305 rank in the ordered list is given by the probability-of-exceedance equation (i.e. the
306 frequency-rank relationship):

307 $$RI = \frac{(n+1)}{m} \tag{2}$$

308 where RI is the recurrence interval (yr), defined as the inverse of frequency (yr^{-1}) or

309 probability of exceedance, n is the total number of samples in each contributing-area and

310 time-interval-of-measurement scaled to units in years (resulting in units of yr), and m is

311 the rank of the magnitude ordered from largest to smallest (unitless). Here the recurrence

312 interval is prescribed (10, 50, 100, and 500 yr), then the rank associated with this

313 recurrence interval is computed using the frequency-rank relationship (Equation 2). The

314 resulting rainfall intensities associated with a user-specified recurrence interval and

315 contributing-area and time-interval-of-measurement class was then used to calculate the

316 Q_p value.

317   At the end of the calculations described above we have datasets of rainfall-

318 intensity values for each combination of the eight contributing-area classes, the seven

319 time-interval-of-measurement classes, and the four recurrence intervals. We then find the

320 maximum values of rainfall intensity associated with a given contributing-area class and

321 recurrence interval among all values of the time-interval-of-measurement class (i.e. the

322 values calculated for 1 to 64 h time intervals). This step is necessary in order to find the

323 maximum values for a given contributing area class and recurrence interval independent

324 of the time-interval-of-measurement, i.e. independent of storm durations and associated

325 types of storms. The maximum values are used to be consistent with the methods of the

326 traditional FECs where the points represent the largest possible storm for a given

327 contributing area. These maximum values are used to calculate Q_p and Q_{fd} (see next

328 section).

329

330 **3.5 Rainfall and Runoff Calculations**

331   The first variable calculated from the maximum rainfall intensities found for each

332 contributing-area class and recurrence interval is the preciptiation (here rainfall only)

333 discharge, Q_p. The variable Q_p is defined as the average rainfall intensity over a basin and

334 time interval of measurement multiplied by the contributing area, resulting in units of m^3

335 s^{-1}. This is a simple calculation resulting in a "discharge" of rainfall to a basin. Q_p is the

336 input value for the flow-routing algorithm that we employ to calculate the peak flood

337 discharge (Fig. 2B, Step 3).

The flow-routing algorithm we employ does not explicitly include infiltration and other losses that can further reduce peak flood discharge relative to input to the basin, Q_p. In this study we modeled infiltration and evaporation losses by simply removing a volume of water per unit time equal to one minus the runoff coefficient, i.e. the ratio of runoff to rainfall over a specified time interval, for three antecedent-moisture scenarios (wet, med, and dry). We estimated runoff coefficients for each contributing-area class and each of three antecedent-moisture scenarios using published values for annual runoff coefficients for large basins within the UCRB and LCRB (Rosenburg et al., 2013) and published values for event-based runoff coefficients for small basins modeled with a range of antecedent-moisture conditions by Vivoni et al. (2007) (Fig. 3). On average, estimated runoff coefficients are higher for smaller and/or initially wetter basins. We found the dependence of runoff coefficients on contributing area and antecedent moisture to be similar despite the large difference in time scales between event-based and annual values. Despite the difference in geographic region between our study site and that of Vivoni et al. (2007) (they studied basins in Oklahoma), the runoff coefficients they estimated are likely to be broadly applicable to the LCRB and UCRB given that basin size and antecedent moisture are the primary controls on these values (climate and soil types play a lesser role except for extreme cases).

We applied the estimated runoff coefficients for all three antecedent-moisture scenarios by simply using them to remove a portion of the Q_p calculated for specific time interval and basin area

$$Q_{pm} = C*Q_p \tag{3}$$

where C is the runoff coefficient calculated for the specific basin area and antecedent-moisture scenario under evaluation. The newly formed Q_{pm} is now the Q_p value for the wet, medium, or dry antecedent-moisture scenario under analysis for each given recurrence interval and contributing area class.

3.6 Flood Discharge Calculations

368   The second variable calculated in this study, and the end-result of our methods, is
369 the peak flood discharge, Q_{fd}. The variable Q_{fd} is the peak flood discharge ($m^3 s^{-1}$)
370 calculated via the diffusion-wave flow-routing algorithm for a hypothetical flood
371 triggered by a rainfall discharge, Q_{pm}, input uniformly over the time interval of
372 measurement to idealized square basins associated with each contributing-area class (Fig.
373 2B, Step 4).

374   The flow-routing algorithm routes flow along the main-stem channel of idealized
375 square basins with sizes equal to the contributing area of each contributing-area class.
376 The choice of a square basin is consistent with the square sample areas (see Section 3.1)
377 and it allows for basin shape to remain the same (and therefore comparable) over the
378 range of contributing areas used in this study. The main-stem channel, with a length of L
379 (m), was defined as the diagonal distance from one corner to the opposite corner across
380 the square basin (i.e. L is equal to the square root of two times the area of the square
381 basin). This main-stem channel was used in conjunction with a normalized area function
382 to represent the shape of the basin and the routing of runoff through the drainage basin
383 network. By including the normalized area function, we can account for geomorphic
384 dispersion (i.e. the attenuation of the flood peak due to the fact that rainfall that falls on
385 the landscape will take different paths to the outlet and hence reach the outlet at different
386 times) in our analyses. The normalized area function, $A(x)$ (unitless), is defined as the
387 portion of basin area, $A_L(x)$ (m^2), that contributes flow to the main-stem channel within a
388 given range of distances (x) from the outlet, normalized by the total basin area, A_T (m^2;
389 Mesa and Mifflin, 1986; Moussa, 2008). The normalized area function is assumed to be
390 triangular in shape with a maximum value at the midpoint of the main-stem channel from
391 the outlet. Area functions, and related width functions, from real basins used in other
392 studies show this triangular shape in general (Marani et al., 1994; Rinaldo et al., 1995;
393 Veneziano et al., 2000; Rodriguez-Iturbe and Rinaldo, 2001; Puente and Sivakumar,
394 2003; Saco and Kumar, 2008), although not all basins show this shape. The triangular
395 area function has been shown to approximate the average area function of basins and that
396 the peak discharge and time to peak discharge is likely more important to the shape of the
397 flood wave (Henderson, 1963; Rodriguez-Iturbe and Valdes, 1979).

398   A 1-dimensional channel with simplified width and along-channel slope

399   appropriate for channels in the CRB is used to approximate the geometry of the main-

400   stem channel of the idealized basin in the flow-routing algorithm. In addition, values for

401   channel slope, S (m/m), and channel width, w (m), are assigned based on the contributing

402   area of the idealized basin and the results of a least-squares regression to channel-slope

403   and channel-width data from the CRB. We assume here that the assigned channel slopes

404   and widths represent the average value for the entire idealized basin. To find the best

405   approximations for channel slope and width values, we developed formulae that predict

406   average channel slope and channel width as a function of contributing area based on a

407   least-squares fit of the logarithms of slope, width, and contributing area based on

408   approximately 100 sites in the Colorado River Basin (CRB; Fig. 4). The data used in

409   these least-squares regressions included slope, width, and contributing area information

410   from all sites in the LCRB and southern UCRB presented in Moody et al. (2003) and

411   additional sites from USGS stream-gauge sites from across the CRB.

412   The assigned channel slope and width values, together with the values of Q_{pm}

413   modified for each antecedent-moisture scenario, were used to calculate the depth-average

414   velocities, V (m s^{-1}), in hypothetical 1D main-stem channels of idealized square drainage

415   basins corresponding to each contributing-area and time-interval-of-measurement class.

416   In this study, flow velocity is not modeled over space and time, but rather is set at a

417   constant value appropriate for the peak discharge using an iterative approach that solves

418   for the peak depth-averaged flow velocity, uses that velocity to compute the parameters

419   of the diffusion-wave-routing algorithm, routes the flow, and then computes an updated

420   estimate of peak depth-averaged velocity. To calculate the depth-averaged velocity, V, we

421   used Manning's equation, i.e.

422    $$V = \frac{1}{n_M} R^{\frac{2}{3}} S^{\frac{1}{2}},$$ (4)

423   where n_M is Manning's n (assumed to be equal to 0.035), and R is the hydraulic radius

424   (m) calculated with the assigned channel width, and S (m/m) is the assigned channel

425   slope. In order to calculate R, water depth, h, of the peak discharge needed to be

426   determined. In this study h was iteratively solved for based on the peak-flow conditions

427   (i.e. the depth-averaged velocity, V, associated with the peak-flood discharge, Q_{fd}) with h

428   set at 1 m for the first calculation of the flow-routing algorithm. At the end of each

429   calculation, h is recalculated using Manning's equation. These iterations continue until

430   the water depth converges on a value (i.e. the change from the last calculation of h to the

431   next calculation of h is ≤ 0.1 m) corresponding to a specific recurrence interval,

432   contributing-area class, and time-interval-of-measurement class.

433   The method we used to model flow through the main-stem channel is the

434   diffusion-wave flow-routing algorithm. This approach is based on the linearized Saint-

435   Venant equations for shallow-water flow in one dimension. To find a simpler, linear

436   solution to Saint-Venant equations, Brutsaert (1973) removed the acceleration term from

437   the equations, leaving the diffusion and advection terms that often provide a reasonable

438   approximation for watershed runoff modeling (Brutsaert, 1973). Leaving the diffusion

439   term in the flow-routing algorithm includes hydrodynamic dispersion of the flood wave

440   in the calculation of the flood hydrograph. In the case where the initial condition is given

441   by a unit impulse function (Dirac function), the cell response function of the channel, q_d

442   (units of s^{-1}), is given by:

443    $$q_d = \frac{x}{(2\pi)^{1/2} b t_r^{3/2}} \exp\left[-\frac{(x - a t_r)^2}{2 b^2 t_r}\right]$$ (5)

444   where x is the distance along the channel from the location where the impulse is input to

445   the channel, t_r is time since the impulse was input into the channel, and the drift velocity

446   a (m s^{-1}) and diffusion coefficient b^2 (m^2 s^{-1}) are defined as

447    $$a = (1 + a_0)V$$ (6)

448    $$b^2 = \frac{V^3}{gSF^2}(1 - a_0^2 F^2)$$ (7)

449   where F is the Froude number, g is the acceleration due to gravity (m s^{-2}), and a_0 is a

450   constant equal to 2/3 when using Manning's equation (Troch et al., 1994). The large

451   floods modeled in this study are assumed to have critical-flow conditions and therefore

452   the Froude number is set to a constant value of 1.

453   The unit response discharge, q_{fd} (m^2 s^{-1}), at the outlet of a drainage basin can be

454   computed from equations (3)-(5) by integrating the product of the cell response function

455    $q_d(x,t)$ corresponding to a delta-function input of the normalized area function, $A(x)$, i.e.

456   the spatial distribution of rainfall input. The integral is given by

457 $$q_{\mathrm{fd}}(t_{\mathrm{r}}) = \int_{0}^{t_{\mathrm{p}}} \frac{Q_{\mathrm{p}}}{w} dt' \int_{0}^{L} q_{\mathrm{d}}(x, t_{\mathrm{r}} - t') A(x) dx \qquad (8)$$

458 where t_{p} is the time interval of measurement over which the unit impulse input (i.e. Q_{p}) is

459 applied to the idealized square drainage basin, and t_{r} is the time after the input of the unit

460 impulse that is long enough to capture the waxing the waning portions and the flood peak

461 of the flood wave. The final peak discharge value, or Q_{fd} ($\mathrm{m}^3\ \mathrm{s}^{-1}$), was calculated by

462 multiplying the unit discharge q_{fd} ($\mathrm{m}^2\ \mathrm{s}^{-1}$) by the channel width found through the formula

463 derived from CRB data in Figure 4, and then selecting the largest value from the resulting

464 hydrograph.

465

466 **3.7 Estimation of Uncertainty**

467   Confidence intervals (i.e. uncertainty estimates) were calculated to quantify the

468 uncertainty in calculated rainfall intensities and associated Q_{p} and Q_{fd} values. In this

469 study we estimated confidence intervals using a non-parametric method similar to that

470 used to calculate quantiles for flow-duration curves (Parzen, 1979; Vogel and Fennessey,

471 1994). Like quantile calculations, which identify a subset of the ranked data in the

472 vicinity of each data point to estimate expected values and associated uncertainties, we

473 estimated confidence intervals for our predictions based on the difference in Q_{p} values

474 between each point and the next largest value in the ranked list. This approach quantifies

475 the variation in the rainfall intensity value for a given contributing area and recurrence

476 interval. In some cases the calculated uncertainties for rainfall intensities and associated

477 Q_{p} and Q_{fd} values are infinite due to the values being past the frequency-magnitude

478 distribution, i.e. there are not enough samples for these values to be determined and there

479 are no finite numbers to sample. These values are not used in this study.

480   The resulting confidence intervals of rainfall intensity were used to calculate

481 confidence intervals for Q_{p} and Q_{fd}. Confidence intervals for Q_{p} values were equal to the

482 confidence intervals for rainfall intensity propagated through the calculation of Q_{p} (i.e.

483 multiplying by contributing area). Confidence intervals for Q_{fd} values were calculated to

484 be the same proportion of the Q_{fd} value as that set by the rainfall intensity value and it's

485 confidence intervals. For example, if the upper confidence interval was 120% of a

486 rainfall-intensity value, the upper confidence interval for the Q_{fd} value associated with the

487 rainfall-intensity value is assumed to be 120% of the Q_{fd} value. This approach to

488 propagation of uncertainty treats all other variables in the calculations as constants and

489 additional uncertainty related to regression analyses on variables used in the flow-routing

490 algorithm such as slope, channel width, and runoff coefficients was not included.

491

492 **3.8 Testing the Effects of Climate Variability**

493   To quantify the robustness of our results with respect to climate variability, we

494 separated the NEXRAD data into El Niño and La Niña months using the multivariate

495 ENSO index (MEI). All months of data with negative MEI values (La Niña conditions)

496 were run together to calculate the rainfall intensity and Q_p values for contributing areas of

497 16, 256, and 4096 km^2, time intervals of 1 to 64 hours, and for 10-, 50-, 100-, and 500-

498 year recurrence intervals. This was repeated with all months of data with positive MEI

499 values (El Niño conditions). Figure 5 shows the distribution of negative and positive MEI

500 values during the 1996 to 2004 water years used in this study.

501

502 **4. Results**

503 **4.1 Channel Characteristics and Runoff Coefficients**

504   Least-squares regression of channel slopes and channel widths from the CRB

505 versus contributing area was used to estimate channel slope, channel width, and runoff

506 coefficients for each idealized basin of a specific contributing-area class. Channel slope

507 decreases as a power-law function of contributing area with an exponent of -0.30 (R^2 =

508 0.39), whereas channel width increases as a power-law function of contributing area with

509 an exponent of 0.28 ($R^2 = 0.65$; Fig. 4). These results follow the expected relationships

510 among channel slopes, widths, and contributing area, i.e. as contributing area increases

511 the channel slope decreases and the channel width increases.

512   Runoff coefficients for wet, medium, and dry antecedent-moisture conditions all

513 decrease with increasing contributing area following a logarithmic function, with the

514 slope of the line decreasing from wet to dry conditions. The fitness of the line to the data

515 also decreases for the wet to dry conditions, with the R^2 values for wet, medium, and dry

516 conditions equal to 0.78, 0.45, and 0.04, respectively. Runoff coefficients decrease with

517 increasing contributing area due to the increased probability of water loses as basin area

518   increases. Also, as expected, runoff coefficients are highest in basins with wet initial

519   conditions that are primed to limit infiltration and evapotranspiration.

520

521   **4.2   Trends in Rainfall Intensity**

522   Maximum rainfall intensities (i.e. the maximum among all time-interval-of-

523   measurement classes) for each contributing-area class and recurrence interval decrease

524   systematically as power-law functions of increasing contributing area for all recurrence

525   intervals with an average exponent of -0.18 ± 0.06 (error is the standard deviation of all

526   calculated exponents found from a weighed least-squares regression; average coefficient

527   of determination $R^2 = 0.78$). Note that maximum-rainfall-intensity results are not

528   presented because they are closely related to the plots of Q_p versus contributing area in

529   Figure 6, i.e. Q_p is simply the rainfall intensity multiplied by the contributing area. The

530   decrease in maximum rainfall intensity with contributing area can be seen in Table 1,

531   where maximum rainfall intensities over contributing areas of 11,664 km^2 are 45% to 8%

532   of maximum rainfall intensity values for basin areas of 16 km^2 in both the UCRB and

533   LCRB (Table 1). The largest decrease in maximum rainfall intensity values between the

534   smallest and largest contributing areas were found for the largest recurrence interval (e.g.

535   500-year) for both the UCRB and LCRB. The decrease in maximum rainfall intensity

536   with increasing contributing area suggests that there is a spatial limitation to storms of a

537   given rainfall intensity.

538   Differences among maximum rainfall intensities for the four recurrence intervals

539   as a function of contributing area are larger in the UCRB than in the LCRB (Table 1).

540   This larger "spread" in the maximum rainfall intensities in the UCRB relative to the

541   LCRB is also propagated throughout the maximum rainfall and flood discharge

542   calculations. For both the UCRB and LCRB, the difference between the 50- and 100-year

543   recurrence interval values was the smallest (Table 1). These trends show that maximum

544   rainfall intensities vary much more as a function of recurrence interval in the UCRB

545   compared with the LCRB.

546   Maximum rainfall intensities associated with a 10-year recurrence interval are

547   similar in the LCRB and UCRB, while intensities were higher in the UCRB than the

548   LCRB for recurrence intervals of 50-, 100-, and 500-years (Table 1). The results of the

549 comparison between the two basins suggest that common (i.e. low-recurrence-interval)

550 rainfall events will have similar maximum rainfall intensities in the UCRB and LCRB,

551 but that rare (i.e. high-recurrence-interval) rainfall events will have higher maximum

552 rainfall intensities in the UCRB than in the LCRB for the same recurrence interval.

553 Maximum precipitation intensities associated with the four defined recurrence

554 intervals are similar to previously published values. In general the values we calculate for

555 the LCRB and the UCRB for the 10-, 50-, and 100-year recurrence intervals are on the

556 order of 10s of mm h^{-1}. This is similar to the spread in values reported on precipitation

557 intensity maps for the same duration and recurrence interval in Hershfield (1961).

558 However, the values reported by Hershfield (1961) are slightly higher (by less than 20

559 mm h^{-1}) in the LCRB for the three recurrence intervals and in the UCRB for the 10-year

560 recurrence interval than values calculated in this study. The values calculated here are

561 also broadly consistent with presented precipitation frequency estimates for points within

562 the LCRB and UCRB provided by the NOAA Atlas 14 Point Precipitation Frequency

563 Estimates website (http://hdsc.nws.noaa.gov/hdsc/pfds/pfds_map_cont.html). Due to the

564 difference in how precipitation intensities are measured and how the frequencies are

565 calculated the values are expected to be slightly different but within the same order of

566 magnitude.

567

568

569 **4.3 Trends in Q_p**

570 Maximum precipitation (here only rainfall) discharges (Q_p hereafter) increase

571 with contributing area as power-law functions with an average exponent of 0.82 ± 0.06

572 (error is the standard deviation of all calculated exponents) based on weighed least-

573 squares regressions on the data ($R^2 = 0.98$) for all recurrence intervals and for both the

574 UCRB and LCRB (Fig. 6). These Q_p values for a given contributing-area class and

575 recurrence interval are the largest values taken from the multiple values calculated for

576 each of the seven time intervals of measurement as explained in Section 3.3. By taking

577 the maximum values, the resulting Q_p FMACs approximate the upper envelope of values

578 of a given recurrence interval. In this study the FMAC follows a power-law function that

579 shows that Q_p increases predictably across the range in contributing areas. As with the

580 maximum rainfall intensity results, differences between Q_p values of different recurrence

581 intervals for a given contributing area were larger for the UCRB than the LCRB (Fig. 6).

582   In general, confidence intervals for Q_p values increase with increasing

583 contributing-area class (Table 1 and Fig. 6). The large values of the highest contributing-

584 area classes and highest recurrence intervals show the spatial limitation of the method,

585 meaning that at these contributing-area classes and recurrence intervals the values are

586 sampled from the largest ranked value and have infinite confidence intervals. These

587 values include the 50-, 100-, and 500-year recurrence intervals for the UCRB and the

588 100- and 500-year recurrence intervals for the LCRB at the 11,664 km^2 contributing-area

589 class. These values also include the 100- and 500-year recurrence intervals for the UCRB

590 and the 500-year recurrence intervals for the LCRB at the 4,096 km^2 contributing-area

591 class. Values with infinite confidence intervals are not included in Fig. 6 due to their high

592 uncertainties.

593

594 **4.4 Trends in Q_{fd}**

595   Maximum Q_{fd} values (hereafter Q_{fd}), i.e. the largest values taken for the multiple

596 values calculated for each time interval of measurement for a given contributing-area

597 class and recurrence interval, were used to plot FMACs for wet, medium, and dry

598 conditions for both the UCRB and LCRB (Fig. 7). In general, FMACs for Q_{fd} values

599 follow the power-law relationship shown in the Q_p FMACs until contributing areas of

600 ~1,000 km^2, where the curves begin to very slightly flatten or decrease. As with the Qp

601 values, Q_{fd} values representing some of the higher recurrence intervals converge to the

602 same value (i.e. the value corresponding to the highest rainfall intensity for the

603 contributing-area class) at contributing areas of ≈10,000 km^2 the and the confidence

604 intervals become infinite (Table 2). This convergence of Q_{fd} values at the largest

605 contributing areas is due to the reduction in the range of values and the number of

606 samples from which to calculate the associated values for each recurrence interval.

607   In general, The UCRB Q_{fd} FMACs (Fig. 7A, C, and E) are slightly higher in

608 magnitude and span a larger range of magnitudes than the FMACs for the LCRB. For

609 both basins, FMACs for the wet, medium, and dry conditions resulting in the highest,

610   middle, and lowest magnitudes, respectively. This trend is expected due to the lowering

611   of runoff coefficients and available water as conditions become drier.

612   FMACs of Q_{fd} for the LCRB plot below published FECs for the LCRB and U.S.

613   (Fig. 7B, D, F) at low contributing areas, but meet and/or exceed the LCRB FEC for

614   contributing areas above ≈1,000 km^2 and ≈100 km^2 for dry and wet antecedent-moisture

615   conditions, respectively. The FMACs for the LCRB do not exceed the U.S. FEC. All of

616   the FMACs of Q_{fd} for the UCRB exceed the LCRB FEC for wet conditions, with the

617   FMACs of lower recurrence intervals exceeding the curve at higher contributing areas

618   than the FMACs of higher recurrence intervals (Fig. 7A). The 500-year FMAC for wet

619   conditions approximate the U.S. FEC for contributing areas between ≈100 to 1,000 km^2.

620   These results suggests that under certain antecedent-moisture conditions, and in basins of

621   certain contributing areas, the LCRB produces floods that exceed the maximum recorded

622   floods in the LCRB and the UCRB produces floods of magnitudes on par with the

623   maximum recorded floods in the U.S.

624

625   **4.5 The Effects of ENSO on Rainfall**

626   Definitive differences in maximum rainfall intensities and Q_p values were found

627   between months with positive versus months with negative MEI values (Table 3). For

628   very small contributing areas (16 km^2) in the LCRB maximum rainfall intensities and Q_p

629   values are similar during negative and positive MEI conditions. Larger contributing areas

630   (256 and 4,096 km^2) show higher maximum rainfall intensities during negative MEI

631   conditions regardless of recurrence interval. Values of Q_p show the same trend as the

632   maximum rainfall intensity in the LCRB. In the UCRB, maximum rainfall intensities and

633   Q_p values during negative MEI conditions are higher than those during positive MEI

634   conditions regardless of recurrence interval.

635

636   **5.   Discussion**

637   **5.1 Use and Accuracy of NEXRAD Products**

638   NEXRAD products are widely used as precipitation inputs in rainfall-runoff

639   modeling studies due to the spatially complete nature of the data necessary for hydrologic

640   and atmospheric models (Ogden and Julien, 1994; Giannoni et al., 2003; Kang and

641 Merwade, 2011). In contrast to past studies similar in scope to this study (Castellarin et

642 al., 2005; Castellarin, 2007; Castellarin et al., 2009) we did not use rain-gauge data and

643 only used NEXRAD products to determine the FMACs for precipitation and flood

644 discharges. We favor NEXRAD products due to the spatial completeness of the data.

645   Intuitively, NEXRAD products that are spatially complete and that average

646 precipitation over a 4 km by 4 km area would not be expected to match rain-gauge data

647 within that area precisely (due to the multi-scale variability of rainfall), although some

648 studies have tried to address this discrepancy (Sivapalan and Bloschl, 1998; Johnson et

649 al., 1999). Xie et al. (2006) studied a semi-arid region in central New Mexico and found

650 that hourly NEXRAD products overestimated the mean precipitation relative to rain-

651 gauge data in both monsoon and non-monsoon seasons by upwards of 33% and 55%,

652 respectively. Overestimation of precipitation has also been noted due to the range and the

653 tilt angle at which radar reflectivity data are collected (Smith et al., 1996).

654 Underestimation of precipitation by NEXRAD products relative to rain gauge data has

655 also been observed (Smith et al., 1996; Johnson et al., 1999), however.

656   Under- and over-estimation of precipitation by NEXRAD products in relation to

657 rain-gauge data is partly due to the difference in sampling between areal NEXRAD

658 products and point data from rain gauges and partly due to sampling errors inherent to

659 both methods. For example, NEXRAD products include problems such as the use of

660 incorrect Z-R relationships for high intensity storms and different types of precipitation,

661 such as snow and hail (Baeck and Smith, 1998). Also, because of its low reflectivity,

662 snow in the NEXRAD products is measured as if it were light rain (David Kitzmiller,

663 personal communication, January 10, 2012). This means the NEXRAD products likely

664 underestimate snowfall and therefore snowfall is not fully accounted for in this study.

665 Due to snowfall not being included in this study, associated snowpack and snowmelt

666 effects were also not accounted for. Rain gauges can also suffer from a number of

667 measurement errors that usually result in an underestimation of rainfall (Burton and Pitt,

668 2001). In addition, gridded rainfall data derived from rain gauges are not spatially

669 complete and therefore must be interpolated between point measurements to form a

670 spatially complete model of rainfall. It is impossible to discern which product is more

671 correct due to the differences in measurement techniques and errors, but by taking both

672 products and combining them into one, the Stage III NEXRAD precipitation products

673 generate the best precipitation estimate possible for this study. Moreover, it should be

674 noted that 100-year flood magnitude predictions based on regression equations have very

675 large relative error bars (ranging between 37 to 120% in the western U.S.; Parrett and

676 Johnson, 2003) and that measurements of past extreme floods can have significant errors

677 ranging from 25% to 130% depending on the method used (Baker, 1987). As such, even a

678 ~50% bias in NEXRAD-product-derived precipitation estimates is on par or smaller than

679 the uncertainty associated with an analysis of extreme flood events.

680   As stated previously, the NEXRAD precipitation estimates used here do not

681 include snowfall and other non-rainfall precipitation types. In this study we also do not

682 include snowpack information into our flood discharge calculations. The omission of

683 snowpack is a reasonably assumption for our low elevation, warm regions within most of

684 the UCRB and LCRB. However, we acknowledge some of our higher elevation areas at

685 higher latitudes may be underestimating the maximum flood discharge by only including

686 rainfall-derived runoff. If the methodology in this paper were applied to a snowmelt-

687 dominated region, snowpack would need to be added to accurately estimate the

688 maximum flood discharge.

689

690 **5.2 Comparison of FMACs to Published FECs**

691   FMACs of Q_{fd} exhibit a similar shape and similar overall range in magnitudes as

692 previously published FECs, derived from stream-gauge and paleoflood records, for the

693 LCRB and U.S. (Fig. 7). In general, the FMACs exceed or match published FECs at

694 larger contributing areas, and are lower than or on par with published FECs at the

695 smallest contributing areas (Fig. 7).

696   All FMACs except the 500-year recurrence-interval curve for the UCRB under

697 wet conditions are positioned well below the U.S. FEC presented by Costa (1987; Fig.

698 7A). The similarity between the 500-year recurrence interval Q_{fd} FMAC for the UCRB

699 under wet conditions and the U.S. FEC suggests that the U.S. FEC includes floods of

700 larger recurrence-intervals, which are similar in magnitude to the 500-year recurrence-

701 interval floods within the UCRB. The approximation of the U.S. FEC by the 500-year

702 UCRB FMAC is a significant finding due to the fact that the U.S. FEC includes storms

703   from other regions of the U.S. with extreme climatic forcings (i.e. hurricanes, extreme

704   convection storms, etc.).

705   The Q_{fd} FMACs for the LCRB can be directly compared to the FEC for the LCRB

706   presented by Enzel et al. (1993). At contributing areas smaller than approximately 100

707   km^2, Q_{fd} FMACs for wet conditions and all recurrence intervals are positioned below the

708   LCRB FEC, but at larger contributing areas Q_{fd} FMACs exceed or approximate the

709   LCRB FEC. Q_{fd} FMACs calculated for medium and dry antecedent conditions show the

710   same trend, but exceed the LCRB FEC at a larger contributing areas ($\geq$ 1,000 km^2). This

711   comparison suggests that although the FMACs overlap the overall range of flood

712   magnitudes of the LCRB FEC, the two methods are not capturing the same trend for

713   extreme flood discharges and the LCRB is capable of producing floods larger than those

714   on record.

715   The difference in the slope of the FMACs, and specifically the exceedance of the

716   published LCRB FEC, suggests that the two methods are not capturing the same

717   information. This difference may be due to the difference in how the data are sourced for

718   each method. FECs are created as regional estimates of maximum flood discharges and

719   are based on stream-gauging station and paleoflood data. The FECs are then used to

720   provide flood information for the region, including ungauged and unstudied drainage

721   basins. FECs are limited to the number of stream gauges employed by public and private

722   parties and do not include all basins within a region. In general, FECs may underestimate

723   maximum floods in larger basins, relative to smaller basins, because there are a larger

724   number of smaller basins to sample than larger basins. This sample-size problem

725   introduces bias in the record where flood estimates for smaller contributing areas may be

726   more correct than estimates for larger basins. In this study, the regional precipitation

727   information given by the NEXRAD network is used to form the FMAC, therefore taking

728   advantage of the entire region and using precipitation data to calculate flood discharges,

729   rather than directly measuring flood discharges. This sampling scheme allows for much

730   larger sample sizes for the range of contributing areas, therefore minimizing the sample

731   bias of the traditional FEC.

732   This study aimed to introduce the new method of the FMAC and therefore

733   improve upon the traditional methods of the FEC. By calculating FMACs we provide

734   frequency and magnitude information of possible flood events for a given region in

735   contrast to the FECs that only provide an estimate of the largest flood on record. This

736   information is vital for planning and infrastructure decisions and the accurate

737   representation of precipitation and flooding in design-storm and watershed modeling. In

738   addition, the fact that the FMACs match the FECs for large (500-year) recurrence

739   intervals and do not exhibit the same trends suggests that the FMACs are capturing

740   different samples than the FECs. This indicates that by using the NEXRAD products, the

741   FMACs may provide a more inclusive flood dataset for a region (especially ungauged

742   areas) than the traditional stream-gauge records.

743

744   **5.3   Precipitation Controls on the Form of the FEC**

745   Q_p FMACs were shown to have a strong (average $R^2 = 0.93$) power-law

746   relationship between Q_p and contributing area for all recurrence intervals. Figure 8 shows

747   a conceptualized FEC where the concave-down shape is created when the observed

748   envelope curve diverges from the constant positive power-law relationship between Q_p

749   and contributing area. This diversion creates a "gap" between the two curves and

750   indicates that flood discharge is not a simple power-law function of contributing area.

751   Three mechanisms have been proposed to explain the "gap" and characteristic concave-

752   down shape of FECs: (1) integrated precipitation (i.e. total precipitation over an area) is

753   more limited over larger contributing areas compared to smaller contributing areas

754   (Costa, 1987), (2) a relative decrease in maximum flood discharges in larger contributing

755   areas due to geomorphic dispersion (Rodriguez-Iturbe and Valdes, 1979, Rinaldo et al.,

756   1991, Saco and Kumar, 2004), and (3) a relative decrease in maximum flood discharges

757   in larger basins due to hydrodynamic dispersion (Rinaldo et al., 1991). The first

758   explanation, proposed by Costa (1987), suggests that there is a limitation to the size of a

759   storm and the amount of water that a storm can precipitate. The effect of precipitation

760   limitations may be evidenced by the decreasing maximum rainfall intensities with

761   increasing contributing area. However, the strong power-law relationship between Q_p and

762   contributing area for all recurrence intervals indicates that Q_p is, in general, increasing

763   predictably over the range of contributing areas used in this study. Even if precipitation

764   limitations affect the shape of the curve, this single hypothesis does not account for all of

765 the concave-down shape of each FEC suggesting that other mechanisms are important to

766 creating the characteristic shape. However, it is important to note that the importance of

767 each mechanism may be different for different locations.

768

769 **5.4 Climate Variability in the NEXRAD Data**

770   The results from comparing negative and positive MEI conditions in the UCRB

771 and LCRB are generally consistent with ideas about ENSO and how it affects

772 precipitation in the western U.S. In the LCRB, during negative MEI conditions, small,

773 frequent storms have similar or slightly higher maximum rainfall intensities and Q_p

774 values than during positive MEI conditions. This similarity between the two conditions

775 may be explained by the balancing of increased winter moisture during El Niño in the

776 southwestern U.S. (Hidalgo and Dracup, 2003) and increased summer moisture through

777 the strengthening of the NAM system and the convective storms it produces during La

778 Niña conditions (Castro et al., 2001; Grantz et al., 2007). In general, the strengthening of

779 the NAM may explain the higher maximum rainfall intensities and Q_p values during

780 negative MEI conditions in the LCRB. Strengthening of the NAM may be due in part to

781 the large temperature difference between the cool sea surface of the eastern Pacific Ocean

782 and the hot land surface of the southwestern U.S. and northwestern Mexico during La

783 Niña conditions. The large temperature gradient increases winds inland, bringing the

784 moisture associated with the NAM (Grantz et al., 2007). In the UCRB it is during

785 negative MEI conditions, where the highest maximum rainfall intensities and Q_p values

786 for all recurrence intervals occur. This suggests that the UCRB is affected by ENSO

787 much like the northwestern U.S., where wetter winters are affiliated with La Niña and not

788 El Niño conditions (Cayan et al., 1999; Hidalgo and Dracup, 2003). It is important to

789 note that this comparison is of intensity rates and not total precipitated moisture so the

790 MEI condition resulting in wetter conditions is not known.

791   In addition to the ENSO analysis, by investigating previous studies we see that,

792 along with natural yearly precipitation variability, the 1996 to 2004 water years included

793 many atmospheric river events (Dettinger, 2004; Dettinger et al., 2011). It is important

794 that these events were included due to their ability to greatly increase winter precipitation

795 in the UCRB and LCRB (Rutz and Steenburgh, 2012). Atmospheric river events

796   (sometimes known as Pineapple Express events) can also be tied to major Pacific climate

797   modes such as the ENSO (Dettinger, 2004; Dettinger, 2011), the Pacific Decadal

798   Oscillation (PDO; Dettinger, 2004), and the North Pacific Gyre Oscillation (NPGO;

799   Reheis et al., 2012) in southern California. Unfortunately, correlations between

800   atmospheric river events are unknown and/or less clear for the interior western U.S.

801   However, all three of these Pacific climate modes shifted during the 9-year study period

802   in ~1998 to 1999 (Reheis et al., 2012) indicating that both positive and negative

803   conditions of the ENSO, PDO, and NPGO exist in the NEXRAD products used in this

804   study.

805   The presence of distinct trends in maximum rainfall-intensity and Q_p values

806   calculated for negative and positive MEI conditions, as well as the information in the

807   literature on atmospheric river events, indicates the NEXRAD products used in this study

808   incorporate circulation-scale weather patterns. In addition, the patterns in maximum

809   rainfall intensities and Q_p values during different MEI conditions agree with common

810   understanding of the effects of ENSO on the western U.S. and provide evidence that the

811   data and methods used in this paper to analyze precipitation are reliable. This analysis

812   shows that the NEXRAD products worked well in this location and that using radar-

813   derived precipitation products may be useful for identifying precipitation and climatic

814   trends in other locations where the FMAC method can be applied.

815

816   **6.   Conclusions**

817   In this study we present the new FMAC method of calculating precipitation and

818   flood discharges of a range of recurrence intervals using radar-derived precipitation

819   estimates combined with a flow-routing algorithm. This method improves on the

820   traditional FEC by assigning recurrence interval information to each value and/or curve.

821   Also, instead of relying on stream-gauge records of discharge, this method uses up-to-

822   date and spatially complete radar-derived precipitation estimates (in this case NEXRAD

823   products) to calculate flood discharges using flow-routing algorithms. This study presents

824   an alternative data source and method for flood-frequency analysis by calculating

825   extreme (high recurrence interval) event magnitudes from a large sample set of

826   magnitudes made possible by sampling the radar-derived precipitation estimates.

827   The FMACs for Q_p and Q_{fd} for the UCRB were similar to those produced for the

828   LCRB. In general, all recurrence-interval curves followed the same general trend,

829   indicating that the mechanisms of precipitation and flood discharge are similar for the

830   two basins. However, there were some differences between the two basins. Overall, there

831   were larger differences between curves of different recurrence intervals for the UCRB

832   than the LCRB suggesting a larger range in maximum rainfall intensities, and therefore

833   Q_p and Q_{fd}, in the UCRB relative to the LCRB. For both the UCRB and LCRB the 50-

834   and 100-year recurrence interval curves for all precipitation and discharge FMACs were

835   the most similar. This similarity may mean that although historical discharge records are

836   short, having a 50-year record may not underestimate the 100-year flood as much as one

837   might expect. Also, for Q_p and Q_{fd}, low recurrence-interval values were slightly higher in

838   the LCRB than in the UCRB. This relationship was opposite for high recurrence-interval

839   values. This likely points to a general hydroclimatic difference between the two basins,

840   with the LCRB receiving high intensity storms annually due to the NAM and the UCRB

841   receiving more intense and rarer winter frontal storms.

842   Power-law relationships between maximum rainfall intensity, Q_p, and

843   contributing area were also found in this study. Maximum rainfall intensities decreased as

844   a power-law function of contributing area with an average exponent of -0.18 ± 0.06 for

845   all recurrence intervals. Q_p values for all recurrence intervals increased as a power-law

846   function of contributing area with an exponent of approximately 0.82 ± 0.06 on average.

847   Based on the constant power-law relationship between Q_p and contributing area, the

848   "gap" or characteristic concave-down shape of published FEC are likely not caused by

849   precipitation limitations.

850   In general, the FMACs of Q_{fd} calculated in this study are lower than, and exceed,

851   the published FECs for the LCRB at lower and higher contributing areas. All FMACs of

852   Q_{fd} were positioned well below the U.S. FEC except the UCRB 500-year FMAC, which

853   approximated the U.S. FEC during wet antecedent-moisture conditions. All FMACs of

854   Q_{fd} for all moisture conditions in the LCRB closely approximated the same magnitudes

855   as the published LCRB FEC, but exceeded it for larger contributing areas. The higher

856   estimates of flood discharges at larger contributing areas may be the result of the

857   difference of sampling methods and are likely not erroneous and may be proved true by

858   future events.

859   Lastly, the approximately 9 years of NEXRAD products were found to be a good

860   representation of climate in the CRB. This conclusion was made based on differences in

861   precipitation between positive and negative ENSO conditions in both the UCRB and

862   LCRB and additional data found in the literature. In general, the UCRB was found to

863   have a hydroclimatic regime much like that of the northwestern U.S. where El Niño

864   conditions result in lower maximum rainfall intensities and amounts and La Niña

865   conditions result in higher maximum rainfall intensities. The LCRB showed a more

866   complex trend with similar maximum rainfall intensities for both El Niño and La Niña

867   conditions.

868   Here this method is applied to the UCRB and LCRB in the southwestern U.S., but

869   could be applied to other regions of the U.S. and the world with variable climate and

870   storm types where radar-derived precipitation estimates are available. In addition, this

871   study used set values of contributing area, drainage basin shape, time intervals of

872   measurement, and recurrence intervals that can be changed based on the focus of future

873   studies. Other variables such as snowpack, elevation, and land use should be explored in

874   conjunction with this method to better understand controls on precipitation and flooding.

875

References

Baeck, M.L. and Smith, J.A.: Rainfall estimates by the WSR-88D for heavy rainfall events, Weather Forecast., 13, 416-436, 1998.

Baker, V.R.: Paleoflood hydrology and extraordinary flood events, J. Hydrol., 96, 77-99, 1987.

Brutsaert, W.: Review of Green's functions for linear open channels, J. Eng. Mech.-ASCE, 99, 1247-1257,1973.

Buishand, T.A.: Extreme rainfall estimation by combining data from several sites, Hydrologic. Sci. J., 36, 4, doi:10.1080/02626669109492519, 1991.

Burton, G.A., Jr. and Pitt, R.E (Eds).: Stormwater effects handbook: a toolbox for watershed managers, scientists, and engineers, Lewis Publishers, Boca Raton, Florida, 2001.

Cañon, J., González, J., and Valdes, J.: Precipitation in the Colorado River Basin and its low frequency associations with PDO and ENSO signals, J. Hydrol., 333, 252-264, 2007.

Castellarin, A.: Probabilistic envelope curves for design flood estimation at ungauged sites, Water Resour. Res., 43, W04406, doi:10.1029/2005WR004384, 2007.

Castellarin, A., Vogel, R.M., and Matalas, N.C.: Probabilistic behavior of a regional envelope curve, Water Resour. Res., 41, W06018, doi:10.1029/2004WR003042, 2005.

Castellarin, A., Merz, R., and Bloschl, G.: Probabilistic envelope curves for extreme rainfall events, J. Hydrol., 378, 263-271, 2009.

910 Castro, C.L., McKee, T.B., and Pielke, R.A. Sr.: The relationship of the North American
911 Monsoon to Tropical and North Pacific surface temperatures as revealed by observational
912 analyses, J. Climate, 14, 4449-4473, 2001.
913
914 Cayan, D.R., Redmond, K.T., and Riddle, L.G.: ENSO and hydrologic extremes in the
915 western United States, J. Climate, 12, 2881-2893, 1999.
916
917 Costa, J.E.: A comparison of the largest rainfall-runoff floods in the United States with
918 those of the People's Republic of China and the World, J. Hydrol., 96, 101-115, 1987.
919
920 Crippen, J.R. and Bue, C.D.: Maximum flood flows in the conterminous United States,
921 U.S. Geological Survey Water Supply Paper 1887, 1977.
922
923 Dalrymple, T.: Flood-frequency analyses, Manual of Hydrology: Part 3, U.S. Geological
924 Survery Water Supply Paper 1543, 80 p., 1960.
925
926 Dettinger, M.: Fifty-two years of "Pineapple-Express" storms across the west coast of
927 North America, U.S. Geological Survey, Scripps Institution of Oceanography for the
928 California Energy Commission, PIER Energy-Related Environmental Research, CEC-
929 500-2005-004, 2004.
930
931 Dettinger, M.D., Ralph, F.M., Das, T., Neiman, P.J., and Cayan, D.R.: Atmospheric
932 rivers, floods, and the water resources of California, Water, 3, 445-478, 2011.
933
934 Enzel, Y., Ely, L.L., House, P.K., Baker, V.R., and Webb, R.H.: Paleoflood evidence for
935 a natural upper bound to flood magnitudes in the Colorado River Basin, Water Resour.
936 Res., 29, 2287-2297, 1993.
937
938 Etheredge, D., Gutzler, D.S., and Pazzaglia, F.J.: Geomorphic response to seasonal
939 variations in rainfall in the Southwest United States, Geol. Soc. Am. Bull., 116, 606-618,
940 2004.

941

942   Federal Emergency Management Agency: Modernizing FEMA's flood hazard mapping

943   program: Recommendations for using future-conditions hydrology for the National Flood

944   Insurance Program, Final Report, U.S. Department of Homeland Security, 2001.

945

946   Fulton, R.A., Breidenbach, J.P., Seo, D.J., Miller, D.A., and O'Bannon, T.: The WSR-

947   88D algorithm, Weather Forecast., 13, 377-395, 1998.

948

949   Giannoni, F., Smith, J.A., Zhang, Y., and Roth, G., 2003: Hydrologic modeling of

950   extreme floods using radar rainfall estimates, Adv. Water Resour., 26, 195-203, 2003.

951

952   Grantz, K., Rajagopalan, B., Clark, M., and Zagona, E.: Seasonal shifts in the North

953   American Monsoon, J. Climate, 20, 1923-1935, 2007.

954

955   Henderson, F.M.: Some properties of the unit hydrograph, J. Geophys. Res., 68, 4785-

956   4793, 1963.

957

958   Herschy, R.: The world's maximum observed floods, Flow Meas. Instrum., 13, 231-235,

959   2002.

960

961   Hidalgo, H.G. and Dracup, J.A.: ENSO and PDO Effects on hydroclimatic variations of

962   the Upper Colorado River Basin, J. Hydrometeorol., 4, 5-23, 2003.

963

964   Hershfield, D.M.: Rainfall Frequency Atlast of the United States for Durations from 30

965   minutes to 24 hours and periods from 1 to 100 years, U.S. Weather Bureau Technical

966   Paper No. 40, 65 p., 1961.

967

968   Hosking, J.R.M., and Wallis, J.R.: The effect of intersite dependence on regional flood

969   frequency analysis. Water Resour. Res., 24, 588-600, 1988.

970

971 Hosking, J.R.M., and Wallis, J.R.: Regional Frequency Analysis, Cambridge University
972 Press, New York, 283 p., 2005.
973

974 House, P.K. and Hirschboeck, K.K.: Hydroclimatological and paleohydrological context
975 of extreme winter flooding in Arizona, 1993, in: Larson, R.A. and Slosson, J.E. (Eds.),
976 Storm-Induced Geologic Hazards: Case Histories from the 1992-1993 Winter in Southern
977 California and Arizona, Geological Society of America Reviews in Engineering Geology,
978 vol. XI, Boulder, Colorado, 1-24, 1997.
979

980 Johnson, D., Smith, M., Koren, V., and Finnerty, B.: Comparing mean areal precipitation
981 estimates from NEXRAD and rain gauge networks, J. Hydrol. Eng., 4, 117-124, 1999.
982

983 Kang, K. and Merwade, V.: Development and application of a storage-release based
984 distributed hydrologic model using GIS, J. Hydrol., 403, 1-13, 2011.
985

986 Li, Bai: Current status of weather radar data exchange, World Meteorological
987 Organization Workshop on Radar Data Exchange, Exeter, UK, April 2013, 16.IV.2013,
988 2013.
989

990 Marani, M., Rinaldo, A., Rigon, R., Rodriquez-Iturbe, I.: Geomorphological width
991 functions and the random cascade, Geophys. Res. Lett., 21, 2123-2126, 1994.
992

993 Mesa, O.J. and Mifflin, E.R.: On the relative role of hillslope and network geometry in
994 hydrologic response, in: Gupta, V.K., Rodriguez-Iturbe, I., and Wood, E.F., (Eds.), Scale
995 Problems in Hydrology, D. Reidel, Dordrecht, Netherlands,1-17, 1986.
996

997 Miller, A.J.: Flood hydrology and geomorphic effectiveness in the central Appalachians,
998 Earth Surf. Processes, 15, 119-134, 1990.
999

1000   Milly, P.C.D., Betancourt, J., Falkenmark, M., Hirsch, R.M., Kundzewicz, Z.W.,

1001   Lettenmaier, D.P., and Stouffer, R.J.: Stationarity is dead: Whither water management?,

1002   Science, 319, 573-574, 2008.

1003

1004   Moody, T., Wirtanen, M., Yard, S.N.: Regional relationships for bankfull stage in natural

1005   channels of the arid southwest, National Channel Design Inc., Flagstaff, AZ, 38 pp.,

1006   2003.

1007

1008   Morrison, J.E. and Smith, J.A.: Stochastic modeling of flood peaks using the generalized

1009   extreme value distribution, Water Resour. Res., 38(12), 1305

1010   doi:10.1029/2001WR000502, 2002.

1011

1012   Moussa, R.: What controls the width function shape, and can it be used for channel

1013   network comparison and regionalization?, Water Resour. Res., 44, W08456,

1014   doi:10.1029/2007WR006118, 2008.

1015

1016   National Atlas: http://www.nationalatlas.gov/atlasftp.html#hucs00m, last access: 8

1017   August 2014

1018

1019   Niezgoda, S. and West, T. (2012) Relationships between Watershed and Stream

1020   Characteristics and Channel Forming Discharge in Snowmelt Dominated Streams. World

1021   Environmental and Water Resources Congress 2012: pp. 1575-1584.

1022   doi: 10.1061/9780784412312.157

1023

1024   NOAA HDSG: http://dipper.nws.noaa.gov/hdsb/data/nexrad/cbrfc_stageiii.php, last

1025   access: 8 August 2014.

1026

1027   NOAA Atlas 14 Point Precipitation Frequency Estimates:

1028   http://hdsc.nws.noaa.gov/hdsc/pfds/pfds_map_cont.html, last access: 8, June 2016.

1029

1030   Ogden, F.L. and Julien, P.Y.: Runoff model sensitivity to radar rainfall resolution, J.

1031   Hydrol., 158, 1-18, 1994.

1032

1033   Parrett, C. and Johnson, D.R.: Methods for estimating flood frequency in Montana based

1034   on data through water year 1998, U.S. Geological Survey Water-Resources Investigations

1035   Report 03-4308, 2003.

1036

1037   Parzen, E.: Nonparametric statistical data modeling, J. Am. Statist. Assoc.,74, 365, 105-

1038   121, 1979.

1039

1040   Puente, C.E. and Sivakumar, B.: A deterministic width function model, Nonlinear Proc.

1041   Geoph., 10, 525-529, 2004.

1042

1043   RadarEU: http://www.radareu.cz/, last access 1 August, 2014.

1044

1045   Reed, S.M. and Maidment, D.R.: Coordinate transformations for using NEXRAD data in

1046   GIS-based hydrologic modeling, J. Hydrol. Eng., 4, 174-182, 2006.

1047

1048   Reheis, M.C., Bright, J., Lund, S.P., Miller, D.M., Skipp, G., and Fleck, R.J.: A half-

1049   million-year record of paleoclimate from the Lake Manix Core, Mojave Desert,

1050   California, Palaeogeogr. Palaeocl., 365-366, 11-27, 2012.

1051

1052   Rinaldo, A., Marani, A., and Rigon, R.: Geomorphological dispersion, Water Resour.

1053   Res., 27, 513-525, 1991.

1054

1055   Rinaldo, A., Vogel, G.K., Rigon, R., Rodriguez-Itrube, I.: Can one gauge the shape of a

1056   basin?, Water Resour. Res., 31, 1119-1127, 1995.

1057

1058   Rodriguez-Iturbe, I. and Valdes, J.B.: The geomorphic structure of hydrologic response,

1059   Water Resour. Res., 15, 1409-1420, 1979.

1060

1061 Rosenburg, E.A., Clark, E.A., Steinemann, A.C., and Lettenmaier, D.P.: On the
1062 contribution of groundwater storage to interannual streamflow anomalies in the Colorado
1063 River basin, Hydrol. Earth Sys. Sc., 17, 1475-1491, 2013.

1064

1065 Rutz, J.J. and Steenburgh, W.J.: Quantifying the role of atmospheric rivers in the interior
1066 western United States, Atmos. Sci. Lett., 13, 257-261, doi:10.1002/asl.392, 2012.

1067

1068 Saco, P.M. and Kumar, P.: Kinematic dispersion effects of hillslope velocities, Water
1069 Resour. Res., 40, W01301, doi:10.1029/2003WR002024, 2004.

1070

1071 Sankarasubramanian, A. and Vogel, R.M.: Hydroclimatology of the continental United
1072 States, Geophys. Res. Lett., 30, 1363, doi:10.1029/2002GL015937, 2003.

1073

1074 Shedd, R.C. and Fulton, R.A.: WSR-88D precipitation processing and its use in National
1075 Weather Service hydrologic forecasting, in: Proceedings, Engineering Hydrology:
1076 Proceedings of the Symposium Sponsored by the Hydrology Division of American
1077 Society of Civil Engineers, 844-848, 1993.

1078

1079 Sivapalan, M. and Bloschl, G.: Transformation of point rainfall to areal rainfall:
1080 Intensity-duration-frequency curves, J. Hydrol., 204, 150-167, 1998.

1081

1082 Smith, J.A. and Krajewski, W.F.: A modeling study of rainfall rate-reflectivity
1083 relationships, Water Resour. Res., 29, 2505-2514, 1993.

1084

1085 Smith, J.A., Seo, D.J., Baeck, M.L., and Hudlow, M.D.: An intercomparison study of
1086 NEXRAD precipitation data, Water Resour. Res., 32, 2035-2045, 1996.

1087

1088 Soong, D.T., Ishii, A.L., Sharpe, J.B., and Avery, C.F.: Estimating flood-peak discharge
1089 magnitudes and frequencies for rural streams in Illinois, U.S. Geological Survey
1090 Scientific Investigations Report 2004-5103, 162 p., 2004.

1091

Stedinger, J.R., Vogel, R.M., and Foufoula-Georgiou, E.: Frequency Analysis of Extreme Events, in: D.R. Maidment (Eds.), Handbook of Hydrology, Chapter 18, 1993.

Troch, P.A., Smith, J.A., Wood, E.F., and de Troch, F.P.: Hydrologic controls of large floods in a small basin: central Appalachian case study, J. Hydrol., 156, 285-309, 1994.

Veneziano, D., Moglen, G.E., Furcolo, P., Iacobellis, V.: Stochastic model of the width function, Water Resour. Res., 36, 1143-1157, 2000.

Vivoni, E.R., Entekhabi, D., Bras, R.L., and Ivanov, V.Y.: Controls on runoff generation and scale-dependence in a distributed hydrologic model, Hydrol. Earth Sys. Sc., 4, 983-1029, 2007.

Vogel, R.M., and Fennesset, N.M., Flow-duration curves I: New interpretation and confidence intervals, J. Water Resour. Bull., 31, 6, 485-504, 1994.

Wallis, J.R., Schaefer, M.G., Barker, B.L., and Taylor, G.H.: Regional precipitation-frequency analysis and spatial mapping for 24-hour and 2-hour durations for Washington State, Hydrol. Earth Syst, Sc. Discuss., 11, 415-442, 2007.

Wolman, M.G. and Costa, J.E.: Envelope curves for extreme flood events, J. Hydraul. Eng.-ASCE, Discussion, 110, 77-78, 1984.

Xie, H., Zhou, X., Hendricks, J.M.H., Vivoni, E.R., Guan, H., Tian, Y.Q., and Small, E.E.: Evaluation of Nexrad Stage III precipitation data over a semiarid region, J. Am. Water Resour. As., 04055, 237-256, 2006.

1123

1124 **Tables**

1125 Table 1. Maximum rainfall intensity and Q_p for the Upper Colorado River Basin (UCRB)

1126 and Lower Colorado River Basin (LCRB). Note that data are all sampled from time

1127 intervals of measurement ≤ 2 hours.

RI	Area (km^2)	Intensity (mm h^{-1})		Q_p (m^3 s^{-1})	
		UCRB	LCRB	UCRB	LCRB
10	16	28.0 ± 0.0	36.6 ± 0.0	125 ± 0	162 ± 0
10	64	25.4 ± 0.1	32.5 ± 0.0	451 ± 1	578 ± 0
10	144	25.1 ± 1.1	29.5 ± 0.4	1004 ± 44	1182 ± 16
10	256	23.7 ± 0.2	27.3 ± 0.0	1682 ± 13	1944 ± 1
10	1024	19.8 ± 1.5	19.7 ± 0.4	5644 ± 427	5610 ± 114
10	1296	20.7 ± 2.4	21.7 ± 3.5	7439 ± 873	7820 ± 1268
10	4096	15.5 ± 3.0	15.9 ± 0.8	17682 ± 3462	18134 ± 890
10	11664	12.6 ± 1.7	11.0 ± 2.6	40914 ± 5571	35521 ± 8586
50	16	55.9 ± 0.7	56.2 ± 0.1	248 ± 3	250 ± 0
50	64	55.1 ± 1.2	47.7 ± 0.0	980 ± 22	847 ± 1
50	144	55.3 ± 3.5	43.3 ± 0.9	2211 ± 142	1734 ± 38
50	256	54.9 ± 1.4	40.9 ± 0.5	3901 ± 101	2908 ± 32
50	1024	50.8 ± 5.5	33.6 ± 1.4	14449 ± 1569	9560 ± 393
50	1296	50.8 ± 25.0	32.5 ± 3.9	18287 ± 9011	11704 ± 1410
50	4096	27.6 ± 22.2	30.0 ± 5.2	31382 ± 25313	34126 ± 5969
50	11664	21.1*	15.4 ± 8.3	68434*	49764 ± 26874
100	16	92.3 ± 0.3	68.6 ± 0.0	410 ± 1	305 ± 0
100	64	91.9 ± 2.5	54.5 ± 0.2	1635 ± 44	970 ± 3
100	144	90.1 ± 3.0	51.9 ± 1.0	3606 ± 118	2075 ± 41
100	256	88.7 ± 4.3	48.4 ± 0.4	6305 ± 307	3440 ± 27
100	1024	63.8 ± 11.0	42.5 ± 2.2	18155 ± 3139	12085 ± 630
100	1296	78.5 ± 50.1	43.2 ± 7.8	28257 ± 18022	15544 ± 2820
100	4096	40.8*	32.0 ± 10.4	46422*	36425 ± 11803
100	11664	21.1*	20.1*	68434*	65011*
500	16	254.0 ± 0.8	81.9 ± 0.5	1129 ± 3	364 ± 2
500	64	229.0 ± 3.1	68.6 ± 1.5	4071 ± 55	1219 ± 26
500	144	219.1 ± 11.9	68.6 ± 4.7	8762 ± 476	2743 ± 187
500	256	219.4 ± 7.3	68.6 ± 3.4	15600 ± 517	4877 ± 242
500	1024	166.0 ± 44.1	68.6 ± 3.1	47229 ± 12554	19507 ± 884
500	1296	174.6 ± 85.3	65.6 ± 31.3	62862 ± 30696	23624 ± 11279
500	4096	81.6*	53.6*	92844*	60930*
500	11664	21.1*	20.1*	68434*	65011*

1128 * Values with infinite confidence intervals, not used in this study.

1129

1130

1131

1132

1133

1134 Table 2. Maximum Q_{fd} for the Upper Colorado River Basin (UCRB) and Lower Colorado

1135 River Basin (LCRB). Note that data are all sampled from time intervals of measurement

1136 ≤ 2 hours.

RI	Area (km^2)	Wet Q_{fd} (m^3 s^{-1})		Med Q_{fd} (m^3 s^{-1})		Dry Q_{fd} (m^3 s^{-1})	
		UCRB	LCRB	UCRB	LCRB	UCRB	LCRB
10	16	65 ± 0	86 ± 0	36 ± 0	47 ± 0	20 ± 0	26 ± 0
10	64	246 ± 1	263 ± 0	137 ± 0	151 ± 0	75 ± 0	89 ± 0
10	144	465 ± 20	489 ± 7	268 ± 12	290 ± 4	156 ± 7	175 ± 2
10	256	657 ± 5	748 ± 0	388 ± 3	449 ± 0	244 ± 2	283 ± 0
10	1024	2363 ± 179	2194 ± 44	1423 ± 108	1326 ± 27	892 ± 68	820 ± 17
10	1296	2244 ± 263	2384 ± 387	1459 ± 171	1543 ± 250	1010 ± 118	1066 ± 173
10	4096	5594 ± 1095	5304 ± 260	3665 ± 718	3375 ± 166	2507 ± 491	2315 ± 114
10	11664	14603 ± 1966	11048 ± 2670	9010 ± 1213	6978 ± 1687	6105 ± 822	4942 ± 1195
50	16	131 ± 2	131 ± 0	73 ± 1	73 ± 0	41 ± 1	41 ± 0
50	64	553 ± 12	387 ± 0	307 ± 7	222 ± 0	172 ± 4	130 ± 0
50	144	1145 ± 73	720 ± 16	636 ± 41	424 ± 9	355 ± 23	259 ± 6
50	256	1772 ± 46	1119 ± 12	1043 ± 27	676 ± 7	639 ± 16	421 ± 5
50	1024	6127 ± 665	3062 ± 126	3665 ± 398	1928 ± 79	2291 ± 249	1308 ± 54
50	1296	7076 ± 3487	3562 ± 429	4265 ± 2102	2300 ± 277	2682 ± 1321	1571 ± 189
50	4096	15716 ± 12650	8487 ± 1485	9451 ± 7607	5850 ± 1023	6076 ± 4890	4343 ± 760
50	11664	44482*	15700 ± 8478	28783*	10176 ± 5495	19770*	7138 ± 3855
100	16	216 ± 1	160 ± 0	120 ± 0	89 ± 0	67 ± 0	50 ± 0
100	64	924 ± 25	442 ± 1	514 ± 14	255 ± 1	286 ± 8	150 ± 0
100	144	1807 ± 60	860 ± 17	1041 ± 35	508 ± 10	610 ± 20	309 ± 6
100	256	2888 ± 140	1324 ± 10	1706 ± 83	798 ± 6	1037 ± 50	499 ± 4
100	1024	10586 ± 1830	3812 ± 199	6366 ± 1101	2438 ± 127	3979 ± 688	1662 ± 87
100	1296	9564 ± 6100	4713 ± 855	5752 ± 3668	3058 ± 555	3619 ± 2308	2104 ± 382
100	4096	29415*	10319 ± 3344	19095*	6654 ± 2156	13116*	4698 ± 1522
100	11664	59600*	18607*	38667*	12904*	26747*	9609*
500	16	594 ± 2	192 ± 1	330 ± 1	107 ± 1	184 ± 1	59 ± 0
500	64	1855 ± 25	556 ± 12	1068 ± 14	320 ± 7	628 ± 8	188 ± 4
500	144	3631 ± 197	1138 ± 77	2141 ± 116	670 ± 46	1306 ± 71	408 ± 28
500	256	6012 ± 200	1879 ± 93	3618 ± 120	1130 ± 56	2266 ± 75	709 ± 35
500	1024	19049 ± 5059	6139 ± 278	11478 ± 3048	3945 ± 179	7186 ± 1909	2660 ± 120
500	1296	19075 ± 9314	7153 ± 3415	12370 ± 6041	4656 ± 2223	8499 ± 4150	3198 ± 1527
500	4096	43688*	14892*	28354*	10460*	19481*	7800*
500	11664	65705*	23062*	42738*	16198*	29364*	12080*

1137 * Values with infinite confidence intervals, not used in this study.

1138

1139

1140

1141

1142

1143

1144

1145

1146 Table 3. Maximum rainfall intensity and Q_p values for 10, 50, 100, and 500-year

1147 recurrence intervals during negative (neg) and positive (pos) Multivariate ENSO Index

1148 (MEI) conditions within the Lower Colorado River Basin (LCRB) and Upper Colorado

1149 River Basin (UCRB). Note that data are all sampled from time intervals of measurement

1150 ≤ 2 hours.

Basin	MEI	Area (km^2)	Intensity (mm h^{-1})				Q_p (m^3 s^{-1})			
			10 yr	50 yr	100 yr	500 yr	10 yr	50 yr	100 yr	500 yr
LCRB	neg	16	39	56	69	77	175	250	305	343
	neg	256	31	46	53	69	2206	3251	3741	4877
	neg	4096	21	32	43	54	23856	36425	48363	60930
	pos	16	40	64	74	130	179	284	330	576
	pos	256	27	38	47	52	1943	2690	3369	3721
	pos	4096	13	20*	20*	20*	15229	22689*	22689*	22689*
UCRB	neg	16	41	98	162	254	186	435	721	1129
	neg	256	33	101	155	254	2366	7172	11012	18055
	neg	4096	22	34	41	82	25556	39013	46422	92844
	pos	16	26	51	56	74	115	225	248	330
	pos	256	18	40	51	56	1255	2810	3601	4018
	pos	4096	10	26	27*	27*	10822	30034	31044*	31044*

1151 * Values with infinite confidence intervals, not used in this study.

1152

1153

1154

1155

1156

1157

1158

1159

1160

1161

1162

1163

1164

1165

1166

1167   **Figures**
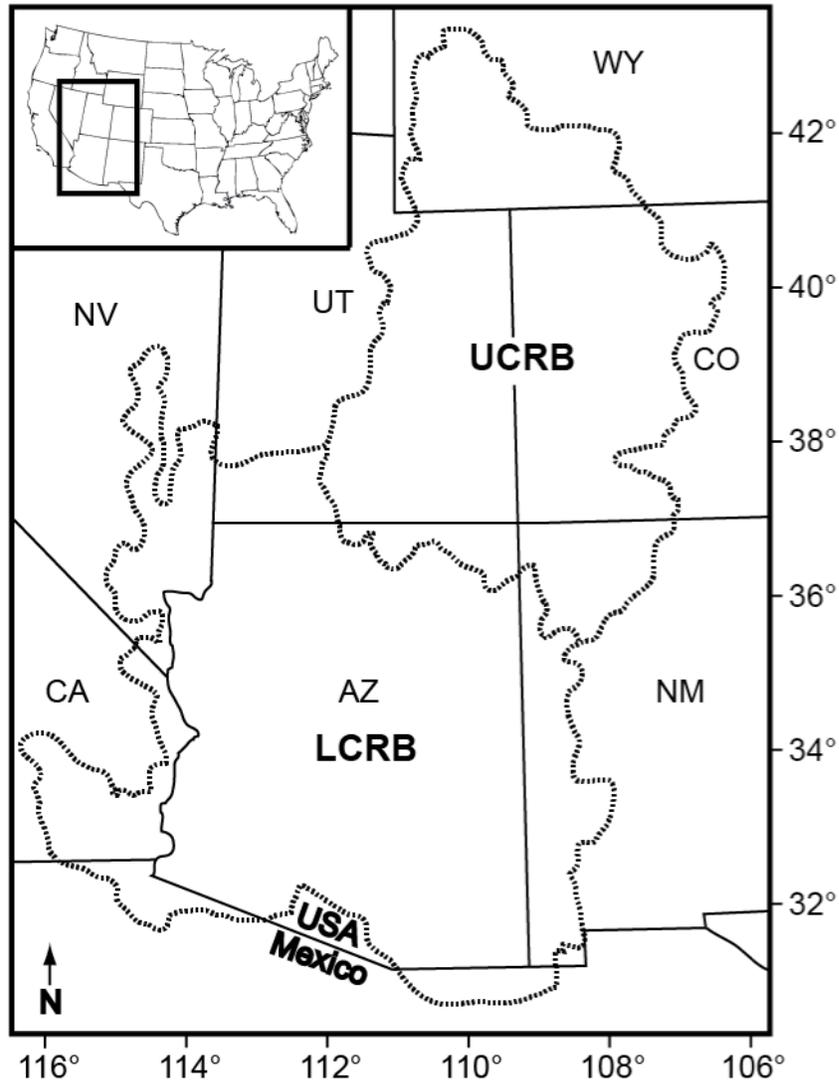
1168
1169   Figure 1. Map showing the locations of the Upper and Lower Colorado River Basins
1170   (UCRB and LCRB, respectively) outlined by the dotted line.
1171
1172
1173
1174
1175
1176
1177
1178

A   **Step 1: Rainfall Sampling Over Space and Time**

For "Time Interval" = 1, 2, 4, 8, 16, 32, 64 h
  Rainfall = Average (Rainfall) into blocks of time of length "Time Interval" (see below)
  For "Area" = 16, 64, 144, 256, 1024, 1296, 4096, 11664 km^2
    For "Basins" within drainage basin defined by user (see below)
      For "Time" 1 to end of 9-year record in increments of "Time Interval"
        Find max Rainfall in consecutive blocks of non-zero Rainfall a.k.a. storm event (see below)
        n = count of max Rainfall values
        Record max storm-event Rainfall ("Time Interval, "Area", n)
      End For "Time" Loop
    End For "Basins" Loop
  End For "Area" Loop
End For "Time Interval" Loop
Result: 7 x 8 x n Array of Rainfall (Time Interval, Area, n)

Example of gridded rainfall intensity aggregated over spatial scales

Example of rainfall intensity averaged over temporal scales

16 km^2 basins   64 km^2 basins

| 0 | 4 | 5 | 7 | 0 | 0 | 7 | 1 | 1-h data
| 2 | | 6 | | 0 | | 4 | | 2-h data
| 4 | | | | 2 | | | | 4-h data
| 3 | | | | | | | | 8-h data
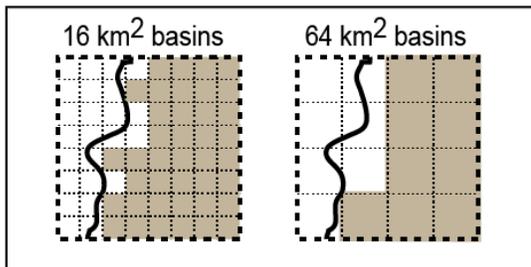
— Study area outline

▨ Basins included (within study area)
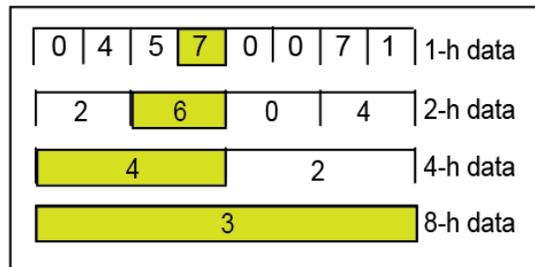
▨ Max Rainfall in Storm Event

Step 2: Rainfall Recurrence Interval Calculations

For "Time Interval" = 1, 2, 4, 8, 16, 32, 64 h
  For "Area" = 16, 64, 144, 256, 1024, 1296, 4096, 11664 km^2
    Rank Rainfall from highest to lowest
    For Recurrence Interval, "RI", = 10, 50, 100, 500 years
      m = (n +1)/"RI" (see Equation 2)
      Record Rainfall at rank m ("Time Interval", "Area", "RI")
    End For "RI" Loop
  End For "Area" Loop
End For "Time Interval" Loop
Result: 7 x 8 x 4 Array of Rainfall (Time Interval, Area, RI)

Figure 2A. Pseudocode describing the methods of the paper with schematic diagrams shown below pseudocode in some cases. Equations within the text and other figures are referenced in red text.

B

Step 3: Q_{pm} Calculation

For Antecedent Moisture Condition, "AMC" = dry, medium, wet
  For "Time Interval" = 1, 2, 4, 8, 16, 32, 64 h
    For "Area" = 16, 64, 144, 256, 1024, 1296, 4096, 11664 km^2
      Runoff Coefficient, RC, set as function of "Area" (see Fig. 3)
      For "RI" = 10, 50, 100, 500 years
        Q_p = Rainfall * "Time Interval" * "Area"
        Q_{pm} = Q_p * RC("AMC") (see Equation 3)
      End For "RI" Loop
    End For "Area" Loop
  End For "Time Interval" Loop
End For "AMC" Loop
Find peak Q_{pm} value from all values for different time intervals and use as max Q_{pm} value
Result: 3 x 8 x 4 Array of Q_{pm} (AMC, Area, RI)

Step 4: Q_{fd} Calculation

For "AMC" = dry, medium, wet
  For "Area" = 16, 64, 144, 256, 1024, 1296, 4096, 11664 km^2
    For "RI" = 10, 50, 100, 500 years
      Slope, S, set as function of "Area" (see Figure 4A)
      Channel Width, W, set as function of "Area" (see Figure 4B)
      For "Iteration" = 1 to when water depth, h, change < 0.001
       If "Iteration" = 1, then h = 1 m
       Else when "Iteration" > 1, then h = last calculated h
       Channel velocity, V = solve Manning's Equation (see Equation 4)
       Drift velocity a = $(1+a_0)V$ (see Equation 6)
       Diffusion coefficient b^2= solve Diffusion Equation (see Equation 7)
        For "Timestep" = 1 to end
         For "Pixel" = 1 to channel length L
          Q_{pm} added to 1D channel following triangular width function A(x)
          Solve Unit Impulse Function q_{fd} (see Equation 5)
          Record peak discharge Q_{fd} ("AMC", "Time Interval", "Area", "RI")
         End For "Pixel" Loop
        End For "Timestep Loop"
       If h change < 0.001, then record peak Q_{fd} ("AMC", "Time Interval", "Area", "RI")
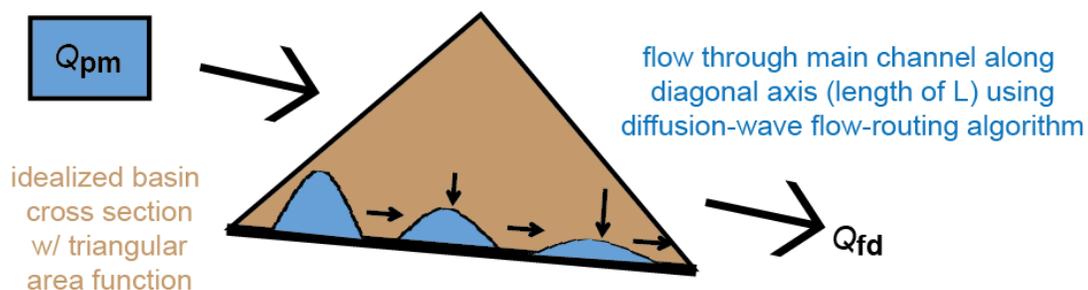   End for "Iteration Loop"
   End For "RI" Loop
  End For "Area" Loop
End For "AMC" Loop
Result: 3 x 8 x 4 Array of Q_{fd} (AMC, Area, RI)

Q_{pm}

flow through main channel along diagonal axis (length of L) using diffusion-wave flow-routing algorithm

idealized basin cross section w/ triangular area function

Q_{fd}

1186

Figure 2B. Pseudocode describing the methods of the paper with schematic diagrams shown below pseudocode in some cases. Equations within the text and other figures are referenced in red text.
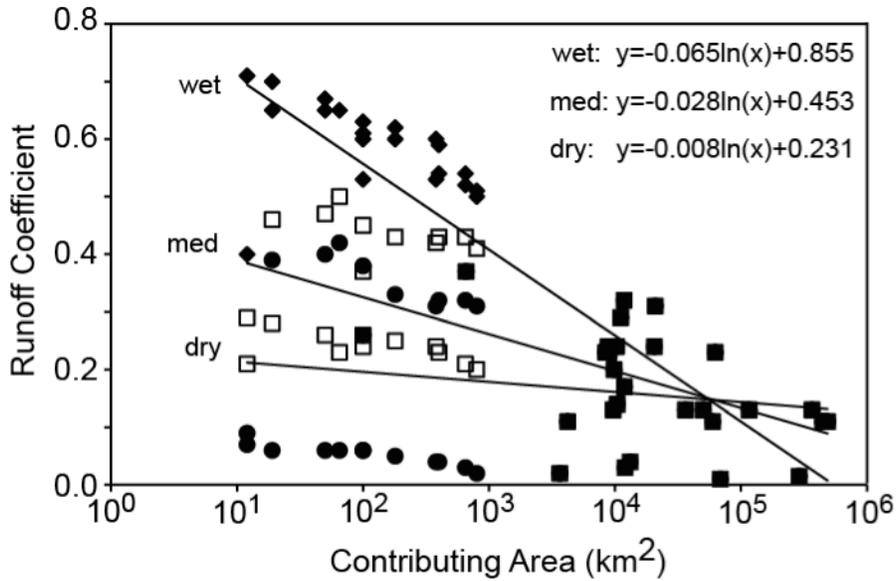
1212

1213 Figure 3. Logarithmic relationships between runoff coefficients and contributing area

1214 using modeled data for wet (filled diamonds), medium (open squares), and dry (filled

1215 circles) antecedent-moisture conditions (Vivoni et al., 2007) and measured data for larger

1216 contributing areas (filled squares; Rosenburg et al., 2013). The medium (open squares)

1217 and dry (filled circles) data separate into two distinct groups relating to the precipitation

1218 event used to model them, with the lower group and higher group relating to a 12-h, 1-

1219 mm h^{-1} event and 1-h, 40-mm h^{-1} event, respectively. All points were used in the least-

1220 squares weighed-regression analysis.

1221

1222

1223

1224

1225

1226

1227

1228

1229

1230

1231

1232
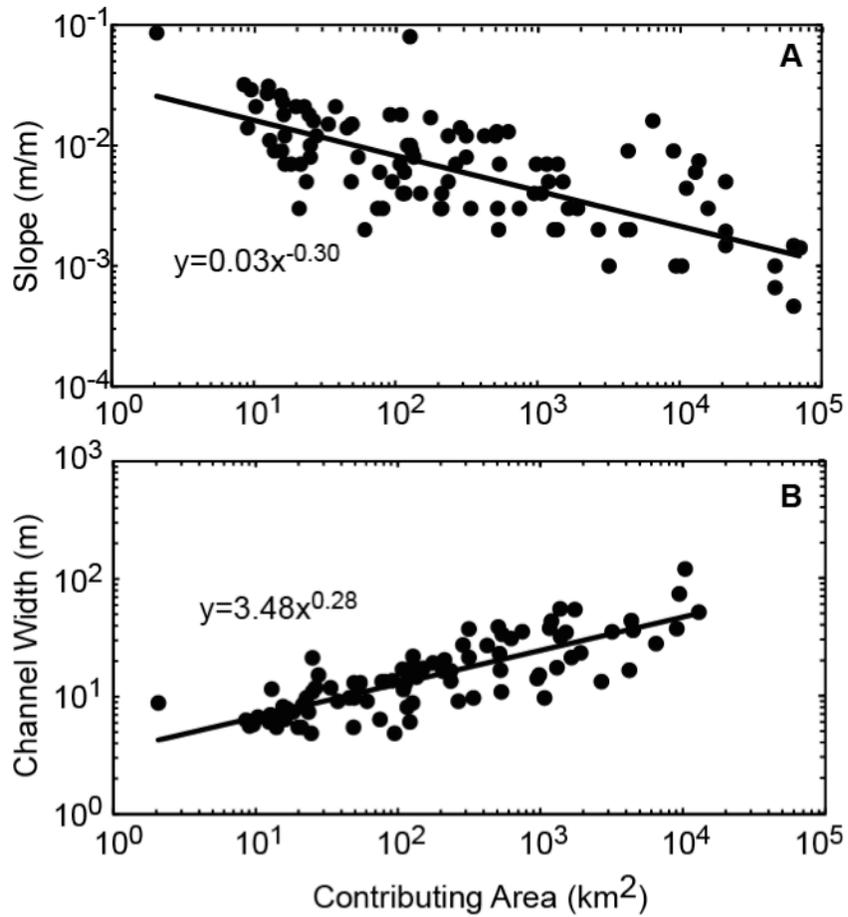
Figure 4. Power-law relationships between channel slope and contributing area (A) and channel width and contributing area (B) for the Colorado River Basin.
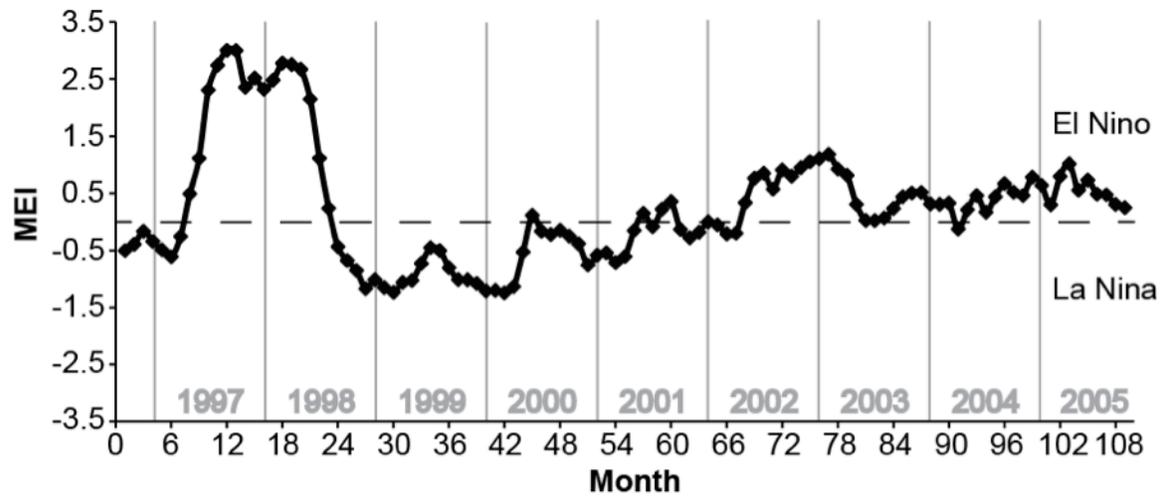
1248

1249   Figure 5. Multivariate ENSO Index (MEI) of months included in Stage III NEXRAD

1250   gridded products. Months are numbered from September 1996 to September 2005 with

1251   years shown in gray. Dashed black line MEI equal to zero. Positive MEI indicates El

1252   Niño conditions, while negative MEI indicates La Niña conditions.

1253

1254

1255

1256

1257

1258
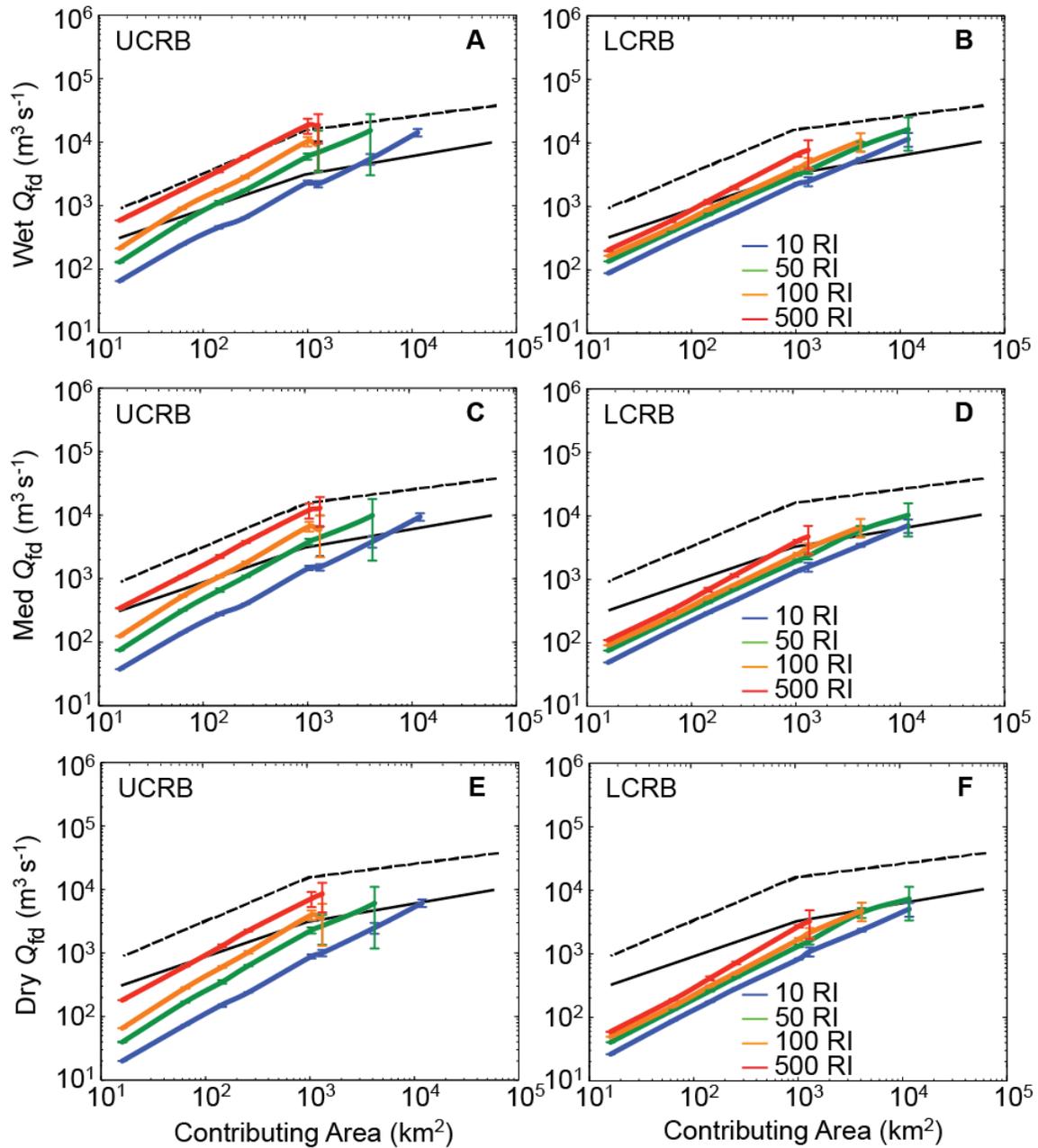
1259

1260

1261

1262

1263

1264

1265

1266

1267

1268

1269

1270
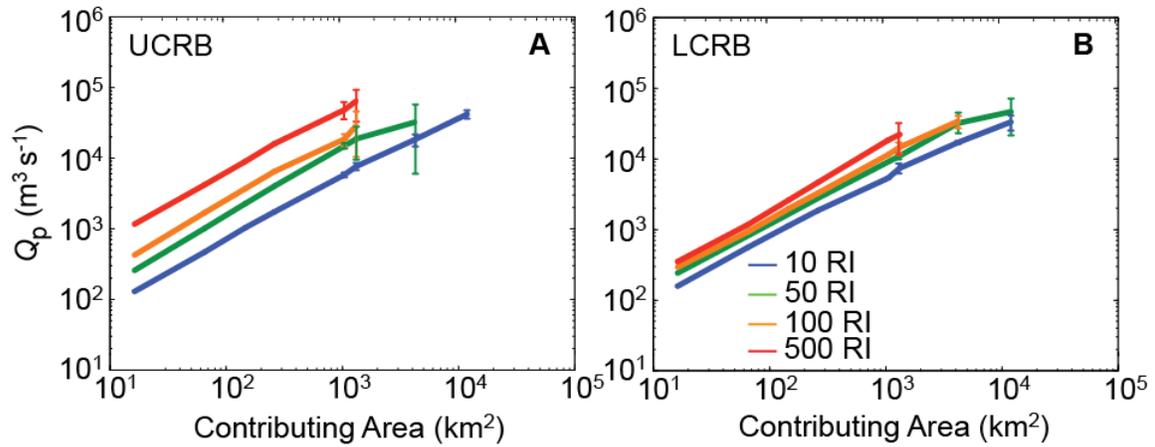
Figure 6. Frequency-magnitude-area (FMA) curves of Q_p versus contributing area for recurrence intervals (RI) of 10, 50, 100, and 500 years for the Upper Colorado River Basin (UCRB; A) and the Lower Colorado River Basin (LCRB; B).

1295

1296   Figure 7. Q_{fd} frequency-magnitude-area curves of 10, 50, 100, and 500 recurrence

1297   intervals (RI) and for wet, medium, and dry conditions for the Upper Colorado River

1298   Basin (UCRB) and the Lower Colorado River Basin (LCRB). Published FECs (black

1299   lines) for the Lower Colorado River Basin (solid black line) from Enzel et al. (1993) and

1300   the United States (dashed black line) from Costa (1987) are also shown.

1301

1302
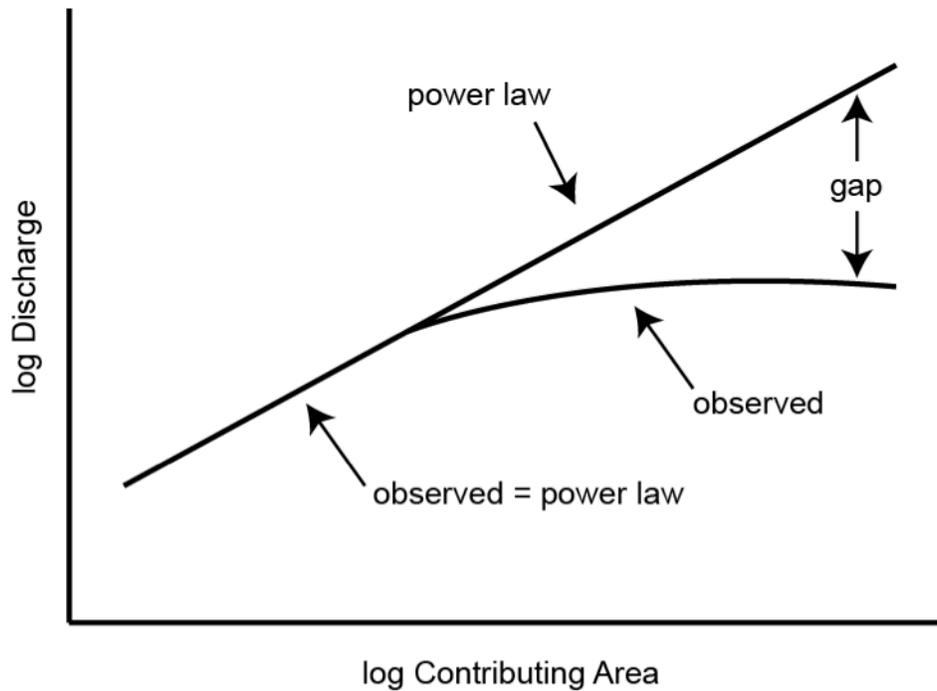
1303

1304   Figure 8. Conceptual diagram of the characteristic concave-down shape of the FEC

1305   (observed) shown in comparison to a power-law function between Q_p and contributing

1306   area. The "gap" between the observed curve and the predicted power law is caused by

1307   precipitation limitations and mechanisms occurring during the routing of water over the

1308   landscape.

1309

1310